Remote Sensing Applications: Society and Environment 37 (2025) 101416

Contents lists available at ScienceDirect

Remote Sensing Applications: Society and Environment

journal homepage: www.elsevier.com/locate/rsase

Remote sensing and gravity investigations for barite detection in Neoproterozoic rocks in the Ariab area, Red Sea Hills, Sudan

Abazar M.A. Daoud [a,b,*], Ali Shebl [a,c], Mohamed M. Abdelkader [a,d], Ali Ahmed Mohieldain [e,f], Árpád Csámer [a,g], Albarra M.N. Satti [b], Péter Rózsa [a]

[a] *Department of Mineralogy and Geology, University of Debrecen, 4032, Egyetem Tér 1, Hungary*
[b] *Faculty of Earth Sciences, Red Sea University, Sudan*
[c] *Department of Geology, Tanta University, 31527, Tanta, Egypt*
[d] *Geology Department, Faculty of Science, Ain Shams University, Egypt*
[e] *Exploration Geosciences Institute, University of Miskolc, Hungary*
[f] *Faculty of Petroleum and Minerals, Al Neelain University, Sudan*
[g] *Cosmochemistry and Cosmic Methods Research Group, University of Debrecen, Debrecen, 4032, Hungary*

ARTICLE INFO

Keywords:
Barite
Remote sensing
Felsic rocks
Enhanced horizontal gradient amplitude (EHGA)
Bouguer anomalies

ABSTRACT

The increasing global demand for barite, driven by its geological importance and various industrial applications, advises the scientific community to improve attempts to identify and explore its deposits in different geological settings. This boost in interest aims to ensure sustainable supply by locating new sources and better understanding the conditions in which barite forms. This study presents an integrated approach using multispectral (Landsat 8 & 9, Sentinel-2, and ASTER) and hyperspectral (PRISMA) remote sensing data, along with geophysical gravity data, to improve the localization of barite deposits. Several image processing methods, including false colour composites, principal component analysis, band ratios, minimum noise fraction, and spectral analysis, were employed for the discrimination of barite deposits, revealing their association with felsic rocks (referred to as group C). Additionally, lineament extraction was performed using the recent and advanced different filters like Tilt Angle Horizontal Gradient (TAHG) and Enhanced Horizontal Gradient Amplitude (EHGA) on Bouguer anomalies, highlighting the structural control of barite deposits by the D3 deformation phase. Field investigations were conducted to validate our findings. Based on these field observations, the integrated methodology successfully mapped the distribution of barite and its host rocks, resulting in an updated geological map for barite distribution that can be used in further exploration phases. We strongly recommend the adopted approach and the newly proposed image combinations for preliminary explorations of barite in similar arid terrains.

1. Introduction

Due to the significance of the high density of barite ($BaSO_4$), it is classified as a critical mineral (Penaloza et al., 2023). Barium sulfate is used in various industries including medical applications for dose reduction and ensuring image quality in computed tomography chest scans (Lee and Kweon, 2020); civil engineering applications for radiation shielding such as barite shielding concrete

---

[*] Corresponding author. Department of Mineralogy and Geology, University of Debrecen, 4032, Egyetem Tér 1, Hungary.
E-mail address: abazar.daoud@science.unideb.hu (A.M.A. Daoud).

https://doi.org/10.1016/j.rsase.2024.101416
Received 5 August 2024; Received in revised form 31 October 2024; Accepted 25 November 2024

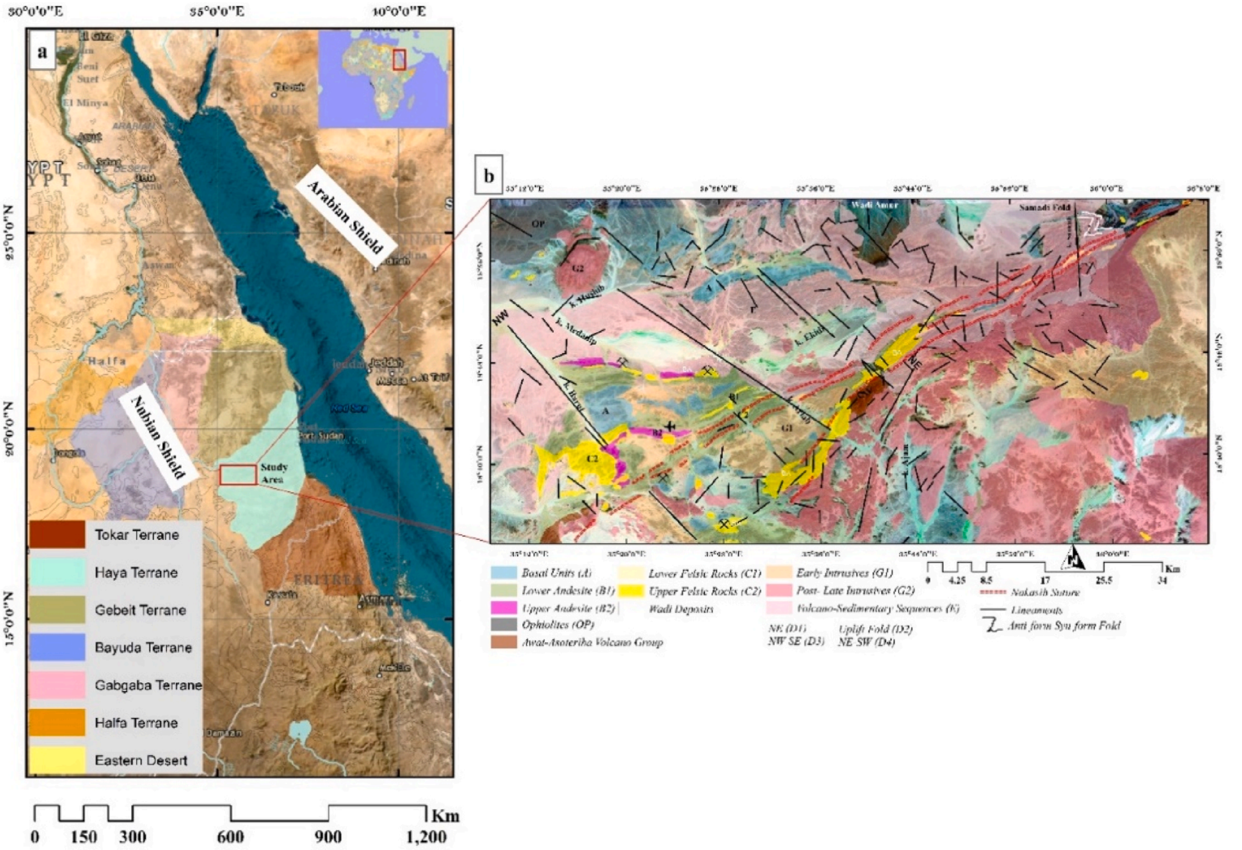

Fig. 1. Location map of the study area; (a) Nubian Shield between Sudan and Egypt, (b) geological map of Ariab area redrawn and modified after Abu-Fatima et al. (2021).

(Daungwilailuk et al., 2022) and as barite aggregates mixed with concrete (Badarloo et al., 2022); in petroleum operations to increase drilling fluid density (Al Jaberi et al., 2022). Moreover, barite deposits have been reported as one of the main primary associations with gold mineralization which occurs as hydrothermal veins (Abu-Fatima et al., 2021; Elsamani et al., 2001; Heijlen et al., 2024).

Recently, lithological mapping and mineral exploration have become fast, non-cost by using integrations of multi-sensor remote sensing and geophysical methods, especially in arid and semi-arid regions such as the Arabian Nubian Shield (Abdelkareem and Al-Arifi, 2021; Bencharef et al., 2022; Elsayed Zeinelabdein et al., 2021; Lu et al., 2022; Mohamed El-Desoky et al., 2021; Shebl and Hamdy, 2023; Zouaghi and Harbi, 2022). These methods provide rapid, detailed insights into subsurface geology. Geophysical techniques, particularly aeromagnetic and gravity data, play a crucial role in mapping lithologies and extracting lineaments in complex terrains. By analyzing corrected Bouguer anomalies using different edge detections, geologists can differentiate between high-density rocks, such as barite and mafic rocks, which produce positive gravity anomalies, and low-density rocks, like sedimentary formations and alluvial deposits, which generate negative anomalies (Abdelsalam and Stern, 1996; Alarifi et al., 2024; H. F. Ali et al., 2024; Bencharef et al., 2022; Eldosouky et al., 2021, 2024; Hirt et al., 2019; Kassa, 2024; Saleh and Gabr, 2024; Sono et al., 2024). This approach is especially valuable in mineral exploration, allowing for a better understanding of lithological variations and structural controls in regions with exciting surface conditions (Eldosouky et al., 2024; Ghoneim et al., 2023; Mahdi et al., 2022).

To date, few studies have investigated and located the distribution of barite deposits using remote sensing techniques, despite the significance of barite and the scarcity of such studies in different geological terrains. However, in recent years, the investigation of barite deposits using multispectral remote sensing techniques has gained significant traction, with foundational studies by (Gajere et al., 2024; Madani and Emam, 2011; Rockwell et al., 2021) leveraging multispectral data to identify and map barium sulfate deposits; for instance (Rockwell et al., 2021), effectively utilized the coastal aerosol band from Landsat 8 (L8) to detect iron sulfate minerals. Building on these improvements, our study not only applies these established remote sensing methodologies but also introduces innovative combinations of multispectral, hyperspectral, and geophysical gravity data (free satellite gravity) to enhance the detection of barite accuracy.

The application of PRISMA hyperspectral data for mineral exploration in the Arabian-Nubian Shield (ANS) represents a groundbreaking advancement, where there has been a notable lack of previous studies using this technology in Sudan (Elrasheed and S, 2024). PRISMA's high spectral resolution allows for precise identification of mineral spectra, distinguishing subtle variations that are crucial for accurate lithological mapping. For example, recent studies have shown PRISMA's effectiveness in detecting alteration minerals and

Table 1
General stratigraphic subdivision of the Red Sea Hills (Abu-Fatima et al., 2021; El-Nadi, 1989).

Stratigraphic column	Subdivision
Post-Pan Africa (<500 M.Y)	Coastal sediments and unconsolidated sedimentary cover
Mainly Mesozoic and Tertiary	Cenozoic volcanics
Pan Africa (890- 500 M.Y)	Anorogenic (ring complexes) syenite, granite, and gabbro
Intrusive	Post-late orogenic intrusive (batholithic)
	Early or syn-orogenic granitoids mainly granites and granodiorites
Pan Africa (900- 500 M.Y)	Meta volcano-sedimentary assemblage, greenschist facies
	Ophiolitic complexes imbricated in the unit above
Pre-Pan Africa (>1200 M.Y)	Amphibolite facies metasediments
	Grey gneisses + granulite group

mapping mineralized zones in arid and inaccessible terrains (Chakraborty et al., 2024; Habashi et al., 2024; Marzouki and Dridri, 2024; Shebl et al., 2024; Sorrentino et al., 2024).

This research aims to fill that gap by developing a comprehensive approach to locate and map barite occurrences; this research integrated comprehensive geospatial analysis and multispectral approach using multi-sensor Landsat 9 (L9), Landsat 8 (L8), Sentinel 2 (S2), Advanced Spaceborne Thermal Emission and Reflectance (ASTER), and PRISMA satellite imagery with an integration of geophysical gravity data to identify and delineate barite deposits within the Ariab area of the Red Sea Hills in Sudan, plateful as a case study. Barite forms fracture-filling and concretions in sandstone, shale, and limestone (Deer FRS et al., 2013), and it is the major accompanying mineral of gold mineralization in Red Sea Hills which usually found as a gangue mineral in metalliferous hydrothermal veins (Abdelrahman et al., 2024; Abu-Fatima et al., 2021).

2. Study area and geological setting

The Ariab area is located in the Red Sea Hills (RSH), a Sudanese part of the ANS which comprises the central part of the Nubian Shield (NS) within the Haya Terrane (Fig. 1). This area was selected because it serves one of the large gold mining companies in Sudan (Ariab Mining Company) with more than 25 open pit mines including Hassai, Hadal Awatib, Adassedakh, Taliaderut, and Hamim.

The Neoproterozoic crust of the NS extends from the Nile Valley in the west to the Red Sea in the east, covering the Red Sea Hills (RSH) (Kröner and Stern, 2004; Stern et al., 1989, 2004; Stern and Kroner, 1993). This crust was formed during the Pan-African Orogeny (PAO) (950–550 Ma), a period marked by the amalgamation of volcanic arcs, intrusive bodies, immature sediments, and ophiolites. These rock associations are characteristic of arc and back-arc basin settings and are primarily found in the green-schist facies (Abdelsalam and Stern, 1993; El-Nadi, 1989; Fritz et al., 2013; Stern and Kroner, 1993).

The ANS itself is divided into several terranes, which are distinct crustal blocks that were accreted during different tectonic events. In the RSH, the terrane division becomes prominent, with six key subzones—Haya, Tokar, Gebeit, Bayuda, Gabgaba, Halfa, and Gelf—each displaying unique tectonic histories. These terranes are separated by ophiolite belts, relics of ancient oceanic crust, which serve as crucial geological markers of the tectonic collisions that shaped the region. These ophiolite belts, trending from east to northeast, formed during the PAO and signify the closing of ocean basins as various terranes collided and accreted (Fig. 1b), (Kröner, 1985; Stern et al., 2004) these terranes consist of quartzite and marble formed approximately 800–900 million years ago, during a period of passive continental margin development (E. A. Ali and Abdel Rahman, 2011).

The Haya terrane (selected study area), formed between 900 and 850 million years ago, hosts the Ariab-Arbaat Belt (Ariab Greenstone Belt) within the southeast Red Sea Hills (RSH). Mostly concealed beneath Phanerozoic sedimentary layers to the west, it is separated from the Gebeit island-arc terrane (830-720Ma) by a NE-trending shear zone delineated by Oshib-Nakasib ophiolite complexes (Abdelsalam and Stern, 1993). The primary rock types in the Haya terrane are green-schist facies of meta-volcano sedimentary sequences separated into two series: Ariab-Arbaat-Tokar to the south and Onib-Nafirdeib to the north. These series evolved from oceanic crust overlain by mafic to felsic volcanics and epiclastic rocks. Intense foliation, green-schist metamorphism, and syn-to late-stage magmatism occurred due to transgressional deformation during accretion along with batholithic granitoids (Abu-Fatima et al., 2021; Adam et al., 2024; Fritz et al., 2013; Vail, 1990).

The initial deformation event, marked by the collision between the Haya and Gebeit terranes, led to the formation of the Nakasib Suture Zone (Fig. 1b) (Abdelsalam, 2010). Subsequently, the arc-continent collision between the ANS and the Saharan Metacraton generated the sinistral Oko Shear Zone, which ultimately truncated the Nakasib Suture Zone (Stern and Abdelsalam, 1998).

In support of this, Abu-Fatima et al. (2021) and El-Nadi (1989) conducted a comprehensive reevaluation of the stratigraphic succession in the RSH. Their work established a more adaptable litho-stratigraphic classification that aligns with the dominant island arc model, which is regarded as the most accurate framework for interpreting the RSH geology. This refined classification, summarized in Table 1, reflects the complex tectonic and volcanic history of the area, providing a more precise geological context for understanding its lithological evolution.

The detailed geology of the Ariab district can be classified into the main five rock units with minor subdivisions of the litho-type units from A, B, C, E, G (Abu-Fatima et al., 2021; Barrie and Hannington, 2019) such as:

Unit A consists primarily of basalt flows with minor occurrences of micro-gabbro and andesitic basalt.

Unit B is an intermediate volcanic unit, characterized by a substantial volcanic presence; subdivisions within Unit B include B1 and B2, which predominantly comprise basaltic andesite to andesite compositions.

Table 2
Summary of tectonic events in the Ariab area (Abu-Fatima et al., 2021).

Cycle and Age	Tectonic and global event
Red Sea Rift (Miocene)	**D4** Fractionation (NE-SW faults), supergene collapse structures. (SBR, Au). Early opening of Red Sea
Pan African (580–730 million years)	**D3** Transgression sinistral (NW-SE to NNW-ESE) and dextral (NNE-SSW) ductile to brittle shear zone. Final collision
(770 Ma)	**D2** Late shortening mainly folding (upright folds), low-grade metamorphism. Mobilization of (Au, Ag, barite). Arc accretion and thickening
	D1 obduction and oblique arc collision (NE trending strike-slip ductile deformation) recumbent to uplift folds.
(900Ma)	**D0** Hydrothermal sub-seafloor metamorphism (Ariab Series (basalt, rhyolite, VHMS, and barite). Primary structures. Juvenile arc in marine environments

Table 3
Spectral sensor characteristics of L8, ASTER, S2, and PRISMA.

Satellite	Bands	Wavelength (nm)	Spectral Region	Spatial Resolution (m)	No. Of Bands
L9 & 8	B1	(430–450)	Coastal aerosol	30	11
	B2	(450–510)	Blue		
	B3	(530–590)	Green		
	B4	(640–670)	Red		
	B5	(850–880)	NIR		
	B6	(1,570–1,650)	SWIR 1		
	B7	(2,110–2,290)	SWIR 2		
	B8	(500–680)	Panchromatic	15	
	B9	(1,360–1,380)	Cirrus	30	
	B10	(10,600–11,190)	TIRS 1	100	
	B11	(11,500–12,510)	TIRS 2		
ASTER	B1	(520–600)	VNIR	15	14
	B2	(630–690)			
	B3N	(780–860)			
	B3B	(780–860)			
	B4	(1,600–1,700)	SWIR	30	
	B5	(2,145–2,185)			
	B6	(2,185–2,225)			
	B7	(2,235–2,285)			
	B8	(2,295–2,365)			
	B9	(2,360–2,430)			
	B10	(8,125–8,475)	TIR	90	
	B11	(8,475–8,825)			
	B12	(8,925–9,275)			
	B13	(10,250–10,950)			
	B14	(10,950–11,650)			
S2	B1	(443)	Ultra-Blue	60	12
	B2	(490)	Blue	10	
	B3	(560)	Green		
	B4	(665)	Red		
	B5	(705)	Red Edge1	20	
	B6	(740)	Red Edge2		
	B7	(783)	Red Edge3		
	B8	(842)	NIR	10	
	B8A	(865)	VNIR (narrow)	20	
	B9	(940)	Water Vapor	60	
	B10	(1375)	SWIR (Cirrus)		
	B11	(1610)	SWIR1	20	
	B12	(2190)	SWIR2		
PRISMA	66 Bands	(400–1010)	VNIR	30	242
	174 Bands	(920–2505)	SWIR		
	PAN			5	

Unit C is a felsic volcanic unit, ranging from rhyodacitic to rhyolitic compositions; subunits within Unit C include: (C1) intercalated within Unit B and contains small lava domes and flows, (C2) the primary host for massive sulfide and **barite deposits** (gold-bearing massive barite and hematite schists) composed of extrusive lavas and pyroclastic material, and (C3) consisting of rhyodacite dykes that cut across all facies of the Ariab Series.

Volcano-sedimentary unit (Unit E), characterized by a significant thickness (several thousand meters) and composed of alternating greywackes, reworked pyroclastic fall deposits, marbles, quartzites, and minor occurrences of carbon-rich cherts and breccia-conglomerates of volcanic origin.

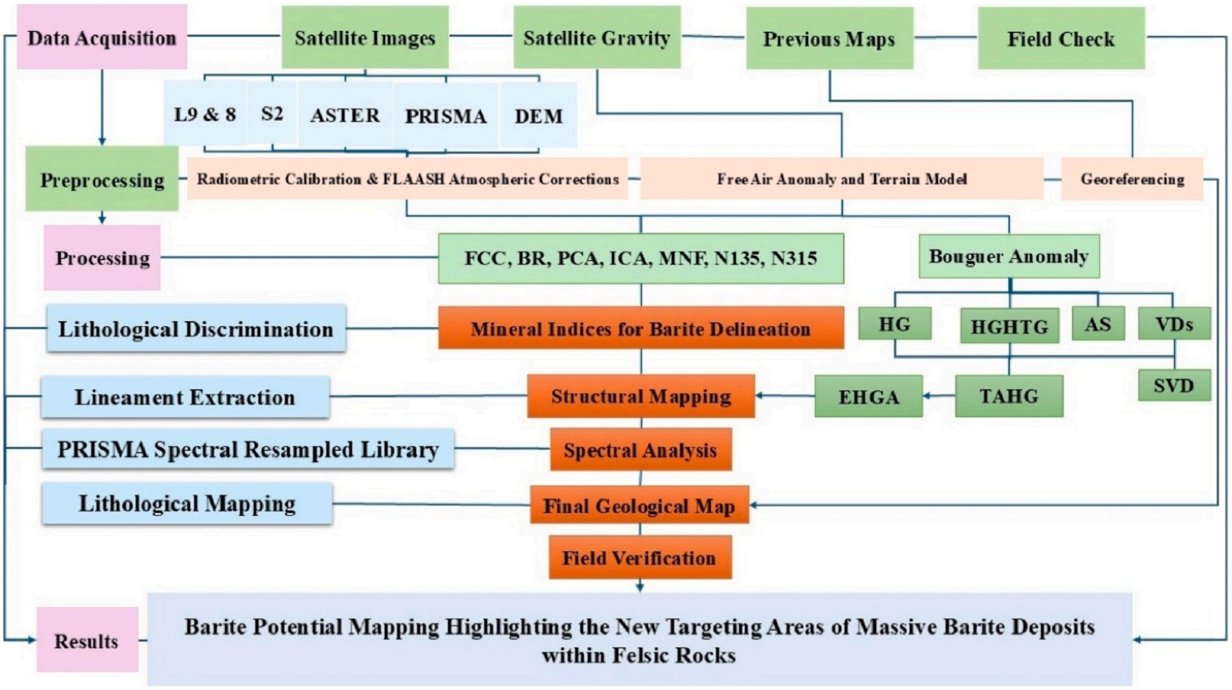

Fig. 2. Flowchart illustrates data and methods used in this study.

Early granitoids intrusives (G) of early (G1) and late (G2) origin constitute up to 40% of the exposed rock formations within the Ariab-Arbaat belt, typically found in the cores of anticlines.

Massive plutons of unaltered equant granodiorite and granite intrude into all members of the Ariab series, including Unit E, exhibiting distinct boundaries and chilled margins (Fig. 1b).

The Ba enrichment is amplified with alteration, particularly in the felsic rocks, (unit C) (Johnson et al., 2003, 2017).

The structural frameworks of the Ariab area are mainly affected by the regional tectonic history of the ANS which are mainly five phases of deformations (D4 to D0) recognized as regional low-grade green-schist facies (Table 2), with the major trending of faults (NE-SW, NNW-SSE, NW-SE, ENE, and NNE) respectively (Abdelsalam, 2010; Abdelsalam and Stern, 1993; Abu-Fatima et al., 2021; Fritz et al., 2013; Johnson et al., 2003; Tucker Barrie, 2009).

Silica Barite Rock (SBR) in the RSH provides a descriptive term for supergene-origin micro-breccias observed as slender lenses adjacent to or expressed by iron oxide-rich facies ‘gossans’ from volcanic massive sulphides (VMS) deposits at the Ariab area with an average of gold content (12 g t^{-1} Au) (Barrie et al., 2016).

3. Data and methodology

3.1. Data

3.1.1. Remote sensing datasets

Advanced Spaceborne Thermal Emission and Reflection Radiometer (ASTER), Landsat 8 and 9 were accessed through USGS, however, Sentinel-2 (S2) were available through the ESA open access hub. In March 2019, the Italian Space Agency launched PRISMA (PRecursore IperSpettrale della Missione Applicativa), a sun-synchronous hyperspectral sensor. PRISMA, a push broom sensor, is equipped with an internal calibration unit, operates at an orbital altitude of 614.8 km with an inclination of 97.751°, and offers a swath width of 30 km, with a spatial resolution of 5 m for panchromatic bands and 30 m for hyperspectral bands. Its spatial and spectral characteristics are given in Table 3. After completing a verification process, registered users can freely access PRISMA data. This access includes both newly acquired and historical data. To ensure equitable access and sustainable use, a daily data usage quota is enforced.

Multi-spectral L9, L8, ASTER, and S2 remote sensing data followed by the hyperspectral Precursor of the Application Mission (PRISMA) for spectral profile analysis were integrated to discriminate the lithological units in the studied terrain and locate barite deposits. All the characteristics of remote sensing datasets are given in Table 1. These data sets are integrated due to their proven efficiency in geological mapping in similar terrains (Gajere et al., 2024; Shebl et al., 2023). A flow chart methodology is introduced in Fig. 2 showing the integration of remote sensing and geophysical methods for lithological mapping and structural analysis required for delineating barite deposits.

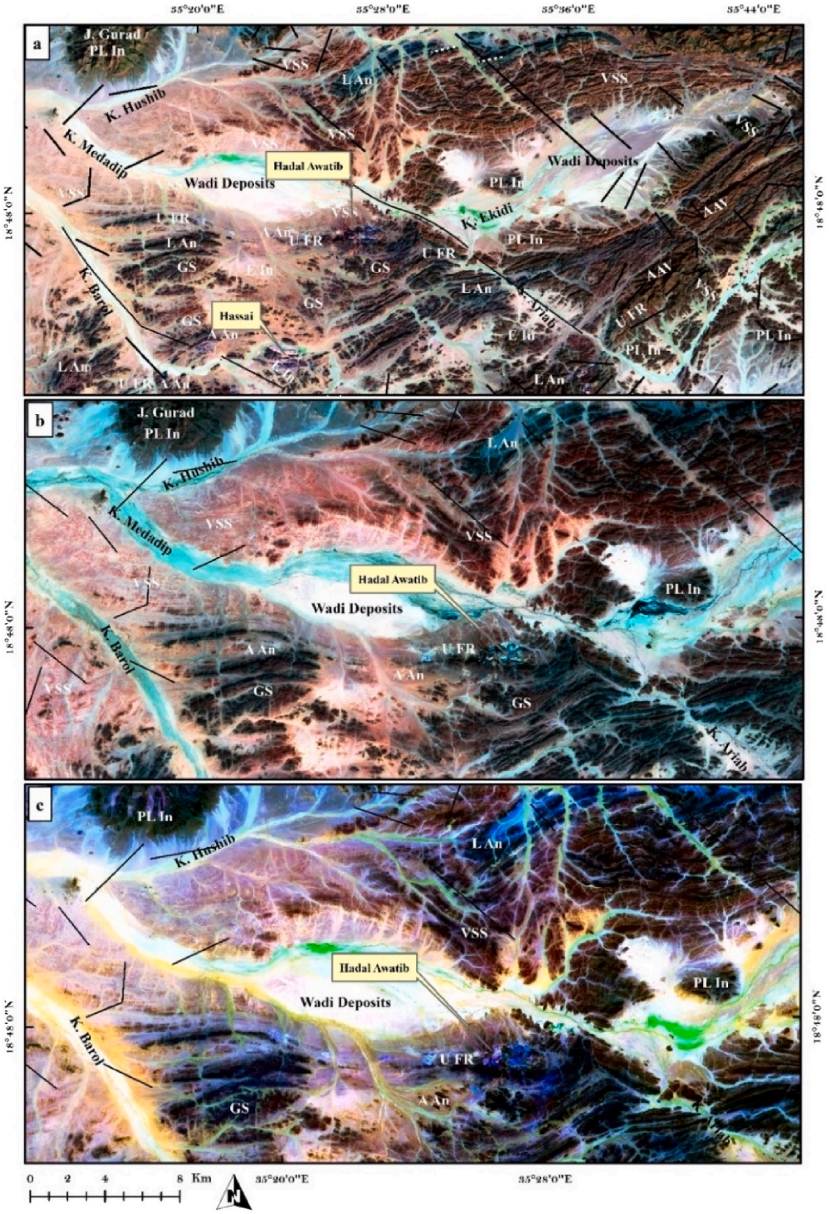

Fig. 3. False colour composite band of (a) L9 7-5-3; (b) ASTER 5-2-1; and (c) S2 12-8A-1 in RGB distinguishing different lithological units (Pln refer to post to late intrusives, Lan: late Andesite, A An: Upper Andesite; UFR: Upper felsic rocks; GS: greenstone facies or basal units; VSS: volcano-sedimentary sequences). (For interpretation of the references to colour in this figure legend, the reader is referred to the Web version of this article.)

3.1.2. *Geophysical gravity data*

The data used for this study is the high-resolution satellite gravity data obtained from the Global Gravity Model plus (GGMplus) as an outcome of collaborative research efforts by Curtin University (Perth) and TU Munich (TUM) which made possible with the support of the Australian Research Council, the TUM Institute of Advanced Study, and the Western Australian iVEC supercomputing facility. The GGMplus integrates three primary components: GOCE/GRACE satellite gravity (covering spatial scales from ~10,000–~100 km), EGM2008 (spanning scales from ~100 to ~10 km), and topographic gravity, which considers the gravitational effect from a high pass filtered terrain model (scales from ~10 km to ~250 m). Coupled with massive parallel computation techniques, this data provides local details at a spatial resolution of 7.2 arc-seconds (~200 m in the North-South direction) (Camacho and Alvarez, 2021; Hirt et al., 2013; Pohan et al., 2023; Rexer et al., 2018). It is available from http://ddfe.curtin.edu.au/gravitymodels/GGMplus/.

GGMplus is used as gravity disturbance data, equal to the free air anomaly. However, to calculate the complete Bouguer anomaly in the study region, we have utilized the latest modern terrain correction model called SRTM2gravity, which was described by (Hirt et al., 2019). SRTM2gravity is a recently developed global model of gravity, which is inferred from the topographic masses on Earth. It can be

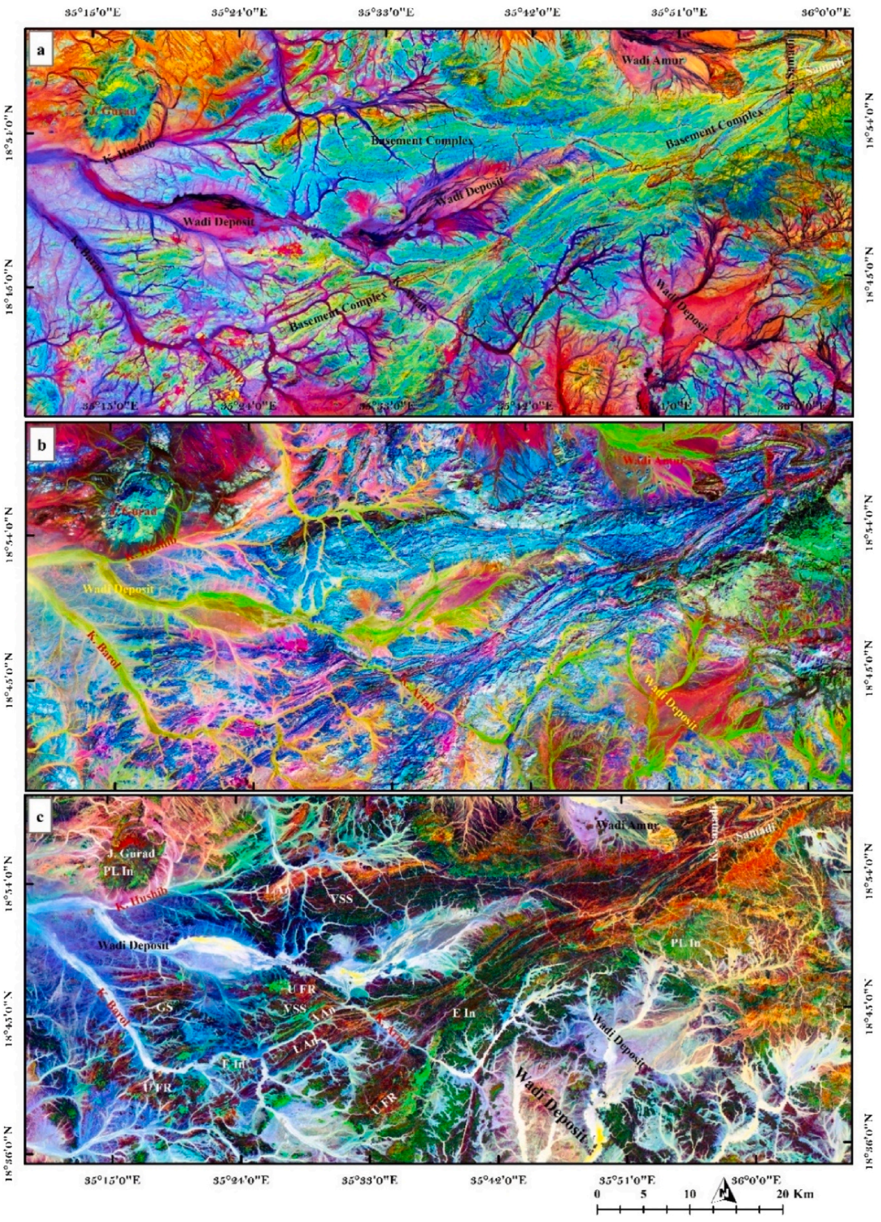

Fig. 4. FCC from BR of L8 (a) (2/1–5/4-7/6–7/5) in RGB distinguishing the basement complex from the Quaternary deposits; (b) bands (6-PC2-6/7) in RGB showing the felsic rocks (unit C) distinctly delineate as purple colour; and (c) (5/4–5/7-3/1) in RGB reveal major distribution of different rock units especially targeting zone appearing as green contrast with barite deposits. (For interpretation of the references to colour in this figure legend, the reader is referred to the Web version of this article.)

considered a contemporary model for gravimetric terrain corrections that depicts the gravitational pull of the worldwide topographic masses of the Earth.

Full-scale topography gravity (in mGal) of the SRTM2gravity products was used to determine the complete Bouguer anomaly of the targeting area. This product can be subtracted directly from GGMplus gravity disturbances hence there is no need to model the gravity effect of a spherical Bouguer shell because it is already incorporated in the full-scale topography gravity.

3.2. Methods

3.2.1. Image processing methods

Specific false colour composites (in RGB) of different spectral bands are applied to L9, L8, ASTER, S2, and PRISMA to create a visually enhanced representation for mapping different rock units within the Ariab district. In this study, we applied dimensionality

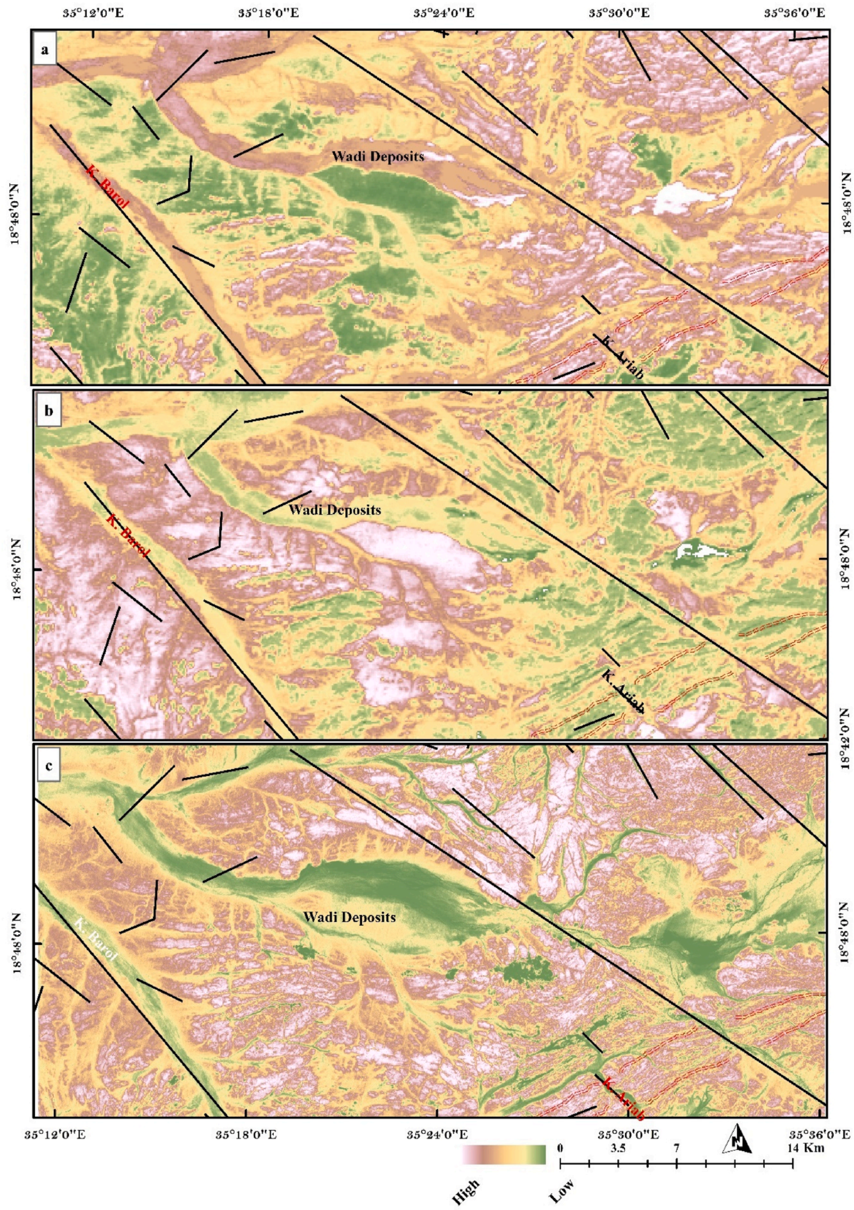

Fig. 5. Distribution of silica-rich minerals: (a) (12/13) in ASTER; (b) S2 (14/12) in S2; and (c) (12/11).

reduction techniques to enhance the visual clarity of satellite images. These enhancements include principal and independent component analyses (PCA & ICA), and minimum noise fraction (MNF). Band ratios were applied by presenting the resulting digital number (DN) values as greyscale or pseudo-coloured images, illustrating relative band intensities obtained by dividing the DN values of one spectral band by the corresponding DN values of another band. Then the generation of multiple combinations of bands and band ratios to distinguish first between the Basement Complex and Quaternary and recent Wadi deposits. They were followed by mapping and targeting indicator minerals such as ferrous, hydroxyl, iron sulfate, and silicate minerals, which are closely associated with barite deposits in the studied terrain. The bands were selected based on their reflectance and absorption properties related to the target features or rocks. Felsic rocks received considerable interest due to their significance in hosting or being associated with barite deposits. After extensive testing of different ratios and trials, we identified the optimal band ratios, which proved to be effective for precise mapping and identification of barite deposits within the study area.

3.2.2. Lineament extraction

The extraction of lineaments is the most important parameter for mapping alteration zones and mineral explorations (Ahmadi et al., 2023; Eldosouky et al., 2022; Es-Sabbar et al., 2020; Shebl and Csámer, 2021). Since there is no specific standard method for

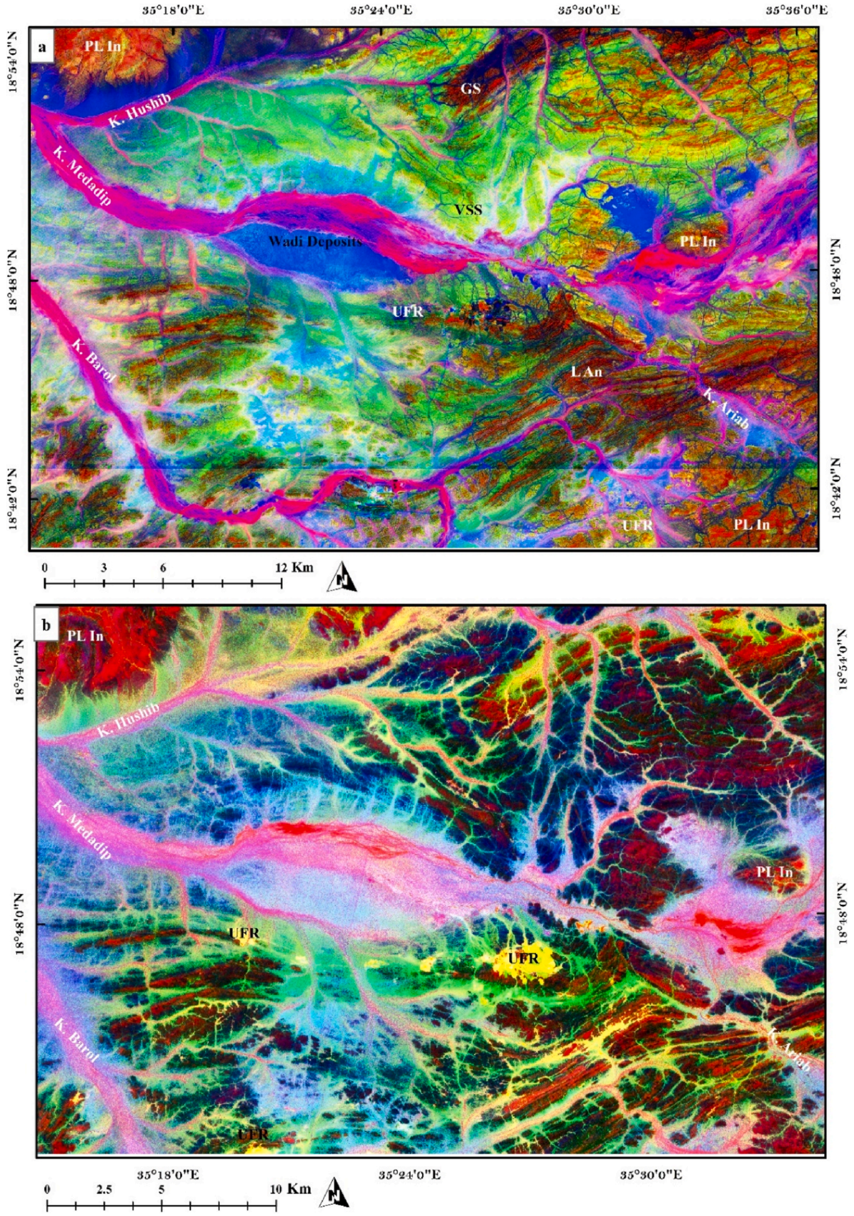

Fig. 6. Precision in delineating the quartz-rich rocks using (a) ASTER PC 6-4-1 showing the volcano-sedimentary rocks appear as green colour (VSS), wadi deposits rich in quartz as pink colour, and red colour for intrusives; (b) S2 (4/2–11/12-4/11 in RGB) discriminating felsic rocks with barite deposits appears as a yellow colour. (For interpretation of the references to colour in this figure legend, the reader is referred to the Web version of this article.)

lineament extraction which is mainly dependent on the geological setting of the selected area and as well as the concept of authors for selecting the proper direction of lineament when we use projected digital elevation model (DEM), Lidar, band 8 in L8, and band ratios, etc., (Laizer et al., 2024; Pratama et al., 2023; Soliman and Han, 2019); we applied two different techniques for lineament mapping including integration of projected digital elevation model (DEM) images and Gravity Gradiometric Mapping Plus (GGMplus).

3.2.2.1. The extraction of lineaments from projected DEM data. Three techniques were applied: redirecting the hill shade in three different orientations (North (N), N135, and N315). The results from these orientations were then merged, which proved to be the most accurate method for lineament extraction in the selected study area.

3.2.2.2. The extraction of lineaments from gravity data. To extract lineaments from satellite gravity data on the Bouguer Anomaly, various filters were applied, including both traditional and advanced methods. These include the Second Vertical Derivative (SVD),

Table 4
Mineral indices and band ratios were used for barite detection in L8, L9, AST, and S2.

Mineral Indications	L 8 & 9	ASTER	S2
Barium sulfate	(B7)/(B4+B2) Rockwell et al. (2021)	(B5/B4) Madani and Emam (2011)	–
Iron sulfate mineral	(B2/B1) - (B5/B4) Rockwell et al. (2021)	–	–
Ferrous iron oxide	(B5/B6) van der Werff and van der Meer (2015)	(B5/B4) Rowan and Mars (2003)	(B12/B8A) + (B3/B4) or (B4/B11) Van der Meer et al. (2014)
Silicates	(B7/B6) –	(B12/B13) Ninomiya and Fu (2019)	(B12/B11) Hewson et al. (2001)
Clay, sulfate, and marble	(B6/B7) - (B5/B4) Rockwell et al. (2021)	–	–
Carbonates	–	(B13/B14) or (B7+B9)/B8 Rowan and Mars (2003)	–
Gossan	B6/B4 Pour et al. (2019)	B4/B2 Pour et al. (2019)	(B6/B8A or B11/B4 van der Meer et al. (2012)
Quartz rich rocks	–	B14/B12 Ninomiya et al. (2005)	–

Horizontal Gradient (HG), Analytic Signal (AS), Tilt Angle (TA), Tilt Angle of the Horizontal Gradient (TAHG), and Enhanced Horizontal Gradient Amplitude (EHGA) filters. Each filter contributes to improved identification and delineation of geological structures (Eldosouky et al., 2024; Ghoneim et al., 2023; Hosseini et al., 2023; Ibraheem et al., 2023; Mahdi et al., 2022), effectively highlighting both shallow and deep-seated geological contacts within the study area. By using this combination of filters, subtle variations in gravity are enhanced, aiding in the precise mapping of structural features critical to the geological assessment (Fig. 2).

3.2.2.3. Second vertical derivative (SVD). The study of vertical derivatives was one of the first techniques used in the interpretation of potential fields (Elkins, 1951), where the vertical derivative is the vertical change of the potential field. It can be calculated from the potential field in various ways. However, the simplest one is the calculation of the second vertical derivative in the frequency domain as:

$$\left\{\frac{\partial^2 g}{\partial z^2}\right\} = k_x^2 f\{g\} + k_y^2 f\{g\} = \left(k_x^2 + k_y^2\right) f\{g\} = |k|^2 f\{g\} \tag{1}$$

Where f { } is the Fourier transform operator, so f {g} is the Fourier transform of the potential field g, k_x, k_y denote the wavenumbers in the x- and y-directions and |k| is the modulus of the wavenumbers.

The second derivative has a higher value at the greatest curvature (crest or trough) and has a zero value where there is no curvature i.e. at point of inflexion; this phenomenon is geologically represented by the existence of faults. SVD also acts as a high-pass filter which enhances high frequencies at the expense of low frequencies it also enhances the noise (Russ and AuthorAnonymous, 2016) however, to solve this issue in geophysical applications it is common to apply some low-pass filters (e.g., Gaussian filters, upward continuations) before the calculation of vertical derivatives to eliminate point noise (Núñez-Demarco et al., 2023). The main objective of applying the SVD in this research study is to delineate shallow faults.

3.2.2.4. Horizontal gradient (HG). Horizontal gradient also known as horizontal derivative is commonly employed as a tool to delineate structures such as faults and geological boundaries (Camacho and Alvarez, 2021; Cordell, 2022; Eldosouky et al., 2020; Núñez-Demarco et al., 2023).

The amplitude of the horizontal gradient is expressed as:

$$HG = \sqrt{\left[\frac{\partial g}{\partial x}\right]^2 + \left[\frac{\partial g}{\partial y}\right]^2} \tag{2}$$

Where (∂g/∂x) and (∂g/∂y) are the horizontal derivatives of the gravity field in the x and y. The method is based on the principle that a near vertical, fault-like boundary produces a gravity anomaly whose horizontal gradient is largest directly over the top edge of the boundary although the method has some limitations (Grauch and Cordell, 1987).

3.2.2.4.1. Analytic signal (AS). AS uses the gradients of the potential field in x, y and z coordinates for source edge detection. It has been utilized by Nabighian (1972) for inferring boundaries of the 2D bodies of a polygonal cross-section, while Roest et al. (1992) proposed the application of the 3D analytic signal to increase the resolution of the boundaries. The amplitude of the analytic signal peaks over the location of density contrasts hence it helps in identifying boundaries, faults or any other structural discontinuity.

The analytic signal is calculated as a sum of the total gradient as follows

$$AS = \sqrt{\left(\frac{\partial g}{\partial x}\right)^2 + \left(\frac{\partial g}{\partial y}\right)^2 + \left(\frac{\partial g}{\partial z}\right)^2} \tag{3}$$

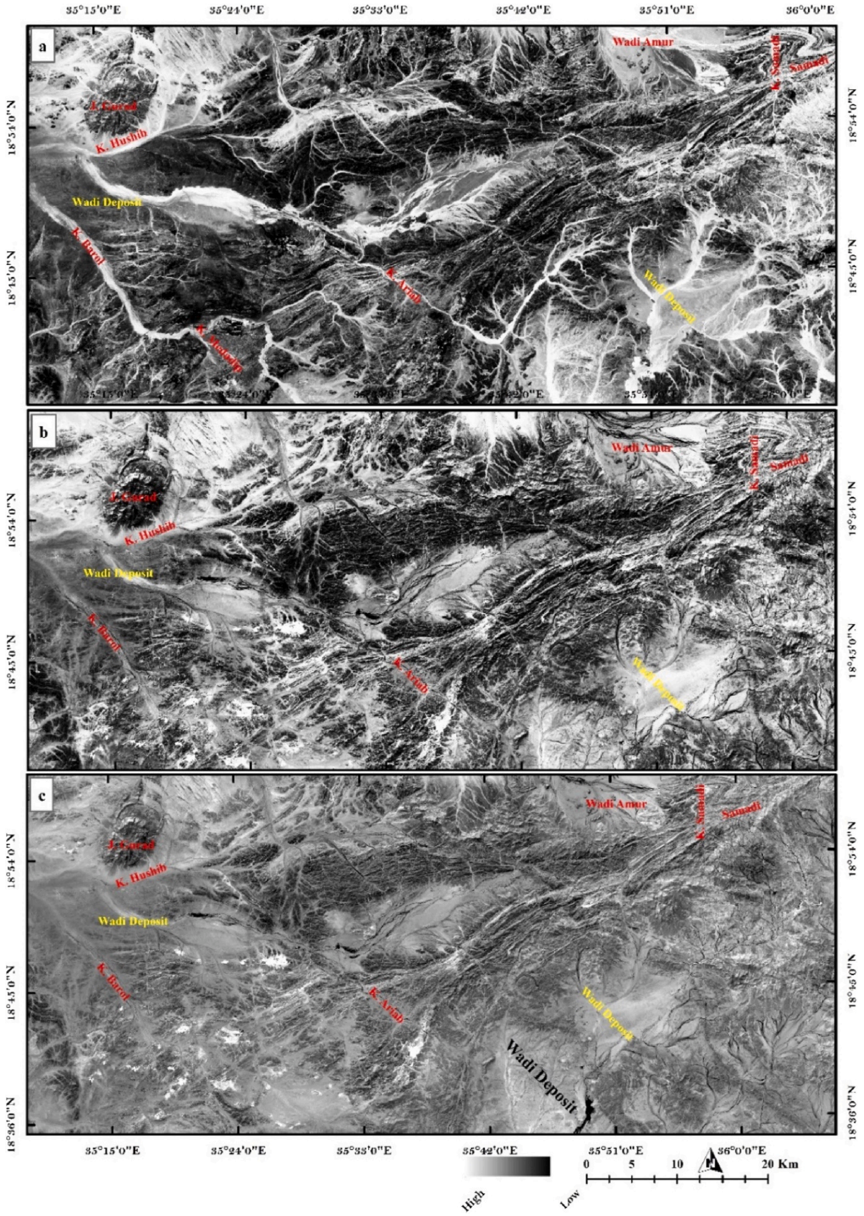

Fig. 7. Greyscale images of band ratios applied to Landsat data showing in bright pixels (a) ferrous oxides (5/6); (b) iron sulfate index (2/1 + 5/4); and (c) high silica and barite content (6/7 + 5/4).

Where (AS) is the amplitude of the analytic signal at (x, y), g is the observed gravity field at (x, y), and ($\partial g/\partial x$, $\partial g/\partial y$ and $\partial g/\partial z$) are the two horizontal and vertical derivatives of the gravity field respectively.

3.2.2.4.2. The Tilt Angle (TA). TA filter introduced by Miller and Singh (1994), is a powerful tool for edge detection in potential field data, such as gravity and magnetic surveys. The filter works by normalizing the vertical gradient of the potential field by its horizontal gradient, providing a measure of the tilt or inclination of the field as:

$$TA = \tan^{-1}\left(\frac{\frac{\partial g}{\partial z}}{\sqrt{\left(\frac{\partial g}{\partial x}\right)^2 + \left(\frac{\partial g}{\partial y}\right)^2}}\right) \tag{4}$$

3.2.2.4.3. The Tilt Angle of the horizontal gradient (TAHG). The TAHG method was introduced by Ferreira et al. (2013). This technique is popular for detecting the horizontal boundaries of buried structures. The edges of buried structures are retrieved by the

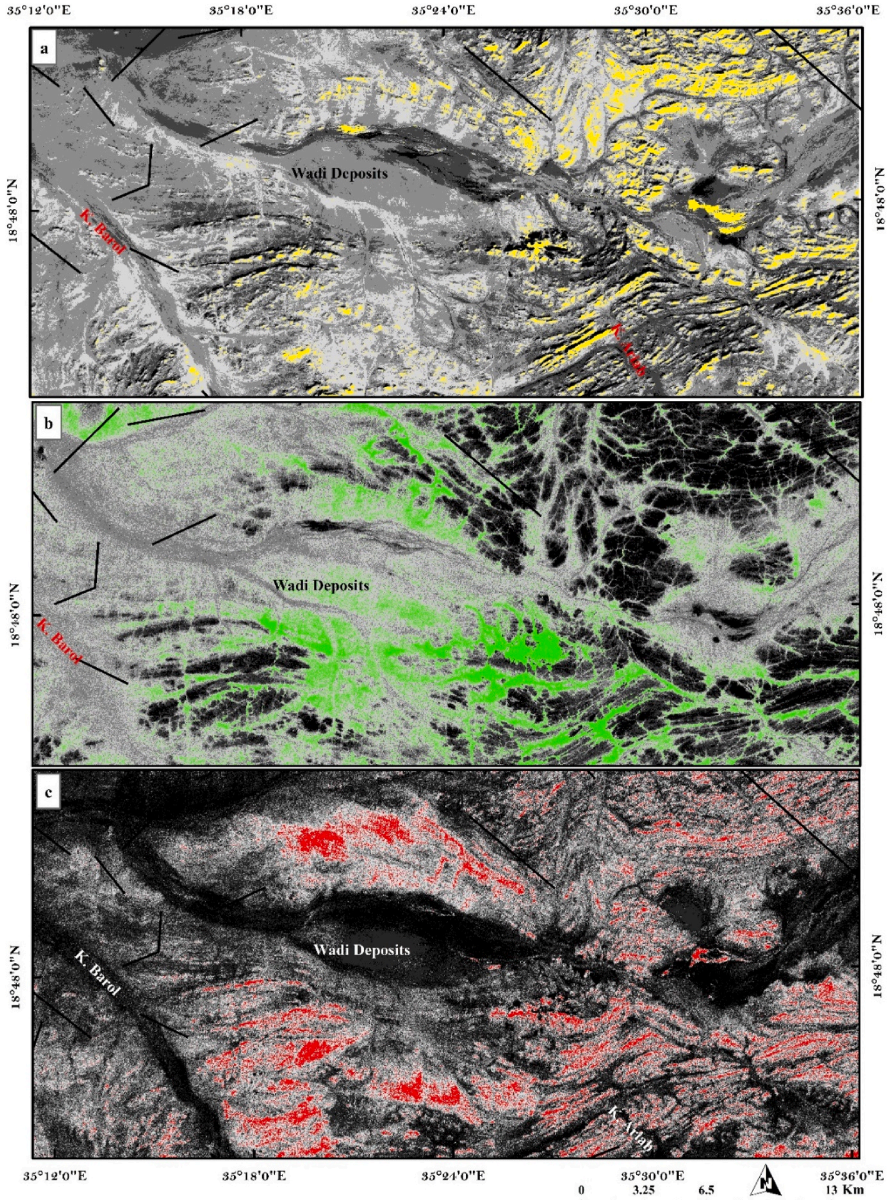

Fig. 8. Band ratios showing the distribution of (a) gossan detected by band ratios of 6/4 in L8; (b) 6/8A in S2; and (c) metasedimentary sequences (unit E) by ASTER bands (7 + 9/8).

maximum values of the TAHG. It can be obtained using the following formula:

$$TAHG = \tan^{-1}\left(\frac{\frac{\partial HG}{\partial z}}{\sqrt{\left(\frac{\partial HG}{\partial x}\right)^2 + \left(\frac{\partial HG}{\partial y}\right)^2}}\right) \tag{5}$$

3.3. The Enhanced Horizontal Gradient Amplitude (EHGA)

The EHGA method was proposed to delineate both the shallow and deep geological contacts responsible for the gravity anomalies observed at the surface (Pham et al., 2020). It can be obtained as follows:

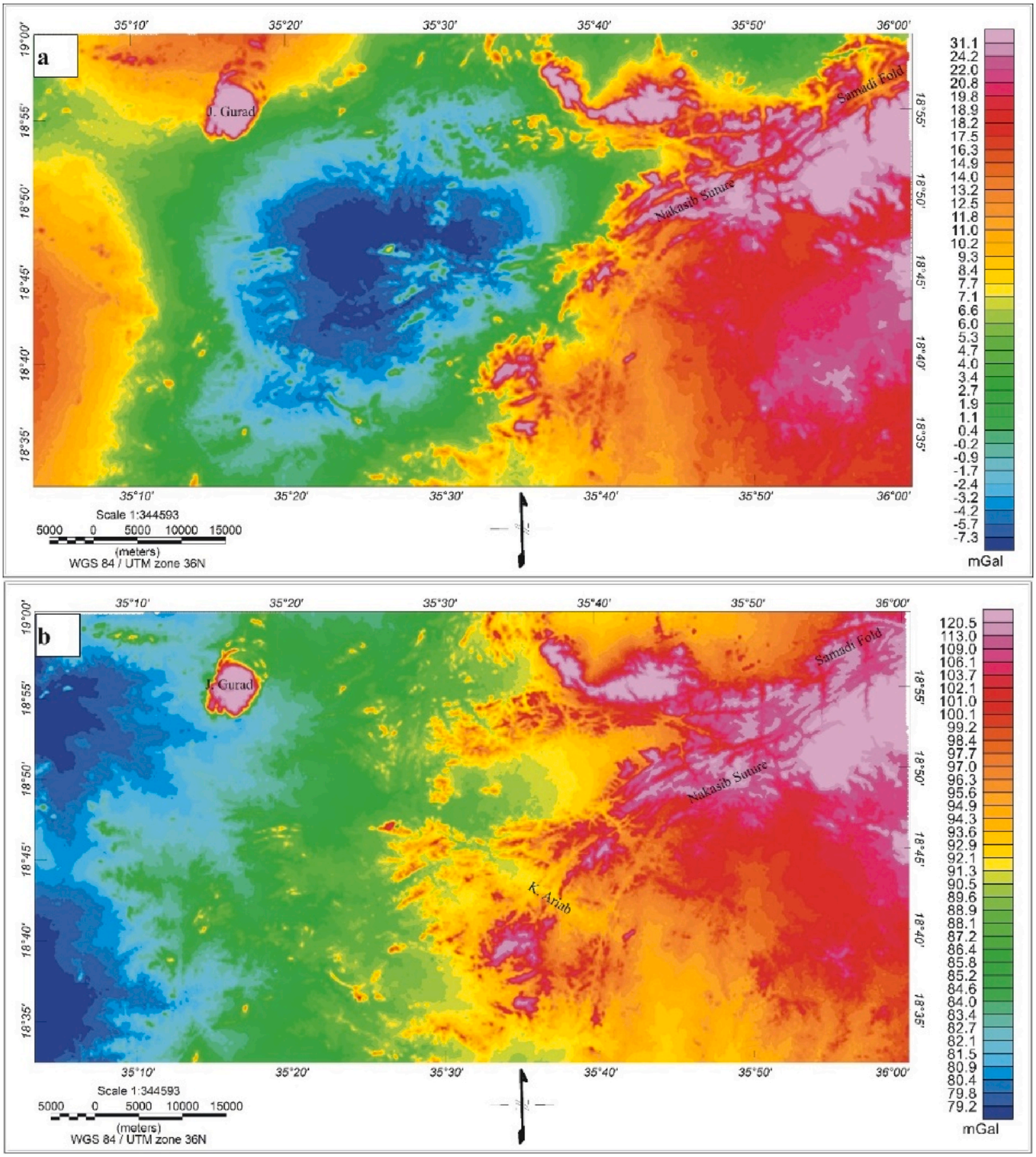

Fig. 9. (a) Free-air anomaly map of the study area; (b) The SRTM2gravity terrain model map.

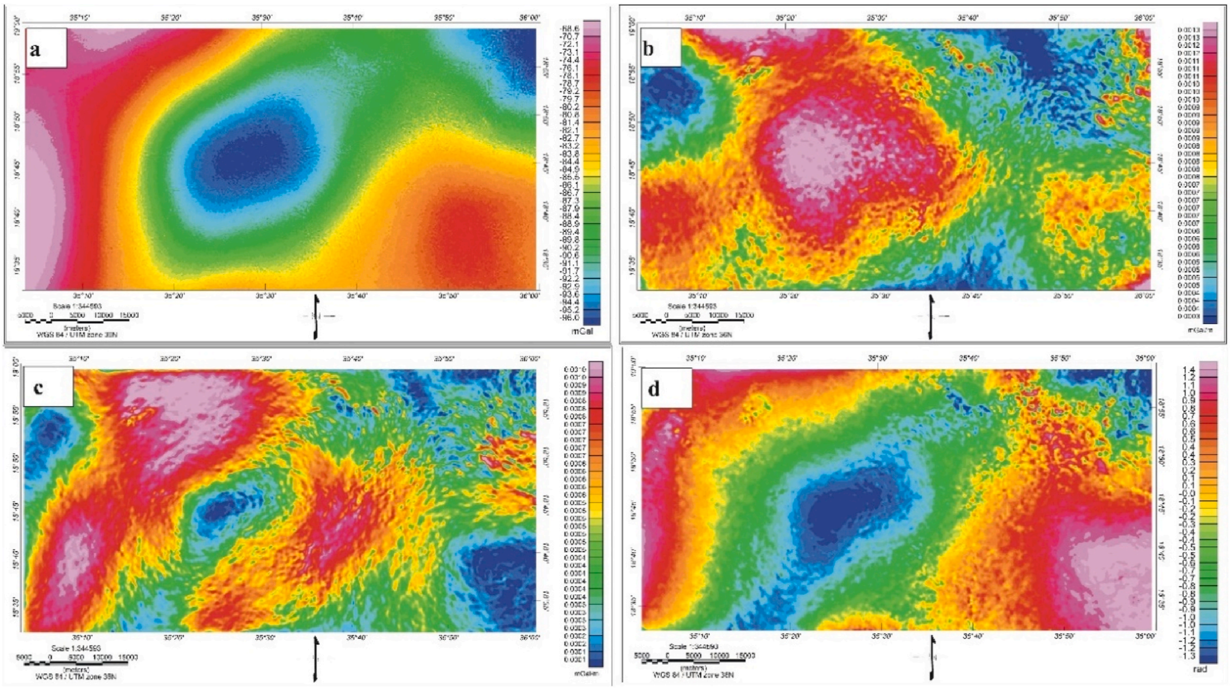

Fig. 10. Maps of (a) Bouguer anomaly (BA); (b) Analytical signal (AS); (c) horizontal gradient (HG); and (d) tilt angle (TA).

$$EHGA = R\left(\operatorname{asin}\left(P\left(\frac{\frac{\partial HG}{\partial z}}{\sqrt{\left(\frac{\partial HG}{\partial x}\right)^2+\left(\frac{\partial HG}{\partial y}\right)^2+\left(\frac{\partial HG}{\partial z}\right)^2}}-1\right)+1\right)\right) \tag{6}$$

Where R is the real part of the function and P is a positive number ≥2. The EHGA ranges from $-\pi/2$ to $+\pi/2$ when the peaks are directly located over the edges.

4. Results

4.1. Precise lithological mapping

FCCs over L9, ASTER, S2, and PRISMA have successfully delineated lithological units in the study area and revealed the well-known lithological groups in the study area known in the previous studies as A, B, C, E, and G. As shown in Fig. 3, basal or greenstone units (A-GS) appears as black colour; andesite rocks (B- LAn) showing dark brown colour; felsic rocks (C- UFR) appears as light brown colour; unit (E– VSS) volcano-sedimentary sequences appear as light brown colour as a major rock unit within the study area; and wadi deposits appear as white, light brown, and dark colour for sand deposits; weathered ferruginous deposits; and weathered basal and andesite units respectively. These detailed lithologies are introduced in Fig. 3 using FCCs of L9 7-5-3, ASTER 5-2-1, and S2 12-8A-1 in RGB respectively. Our results revealed distinct relationships between barite occurrences and specific lithological units with rock unit (C-UFR) as shown in (Fig. 3a, b, and c) respectively. Thus, special consideration is given to lithologies grouped as rock unit C (marked as UFR in Fig. 3).

Before delving into felsic rocks, we began to set apart the other lithologies to ensure better discrimination. For instance, among several combinations, FCC of (2/1–5/4)-7/6–7/5) in RGB was the best to distinguish the basement complex (green-yellow) from the Quaternary deposits (red-pink) using L8 sensor data (Fig. 4a). An image combination of 6-PC2-6/7 in the RGB representation, applied to L8 data clearly depicts the unit (C) or felsic rocks (purple to cyan) as in (Fig. 4b). Furthermore, the additional combination of 5/4–5/7-3/1in RGB reveals the major distribution of different rock units, especially targeting unit (C- UFR) felsic rocks, appearing as green (Fig. 4c).

A bit closer to our target, our investigation of silicate and quartz-rich rocks revealed a reasonable distribution using ASTER and S2 combinations. By using band ratios, specifically thermal (TIR) and shortwave infrared (SWIR) bands as ASTER (12/13) (Fig. 5a), and (14/12) (Fig. 5b), and S2 (12/11) (Fig. 5c), we attained heightened precision in delineating the quartz-rich rocks of unit (C- UFR). Notably, (PC6-4-1 and 4/2–11/12-4/11 in RGB) in ASTER and S2 individually highlight discriminating against the lithological units containing silica and quartz rocks (Units C, E, A) within the study area as illustrated in (Fig. 6a and b). Our results effectively

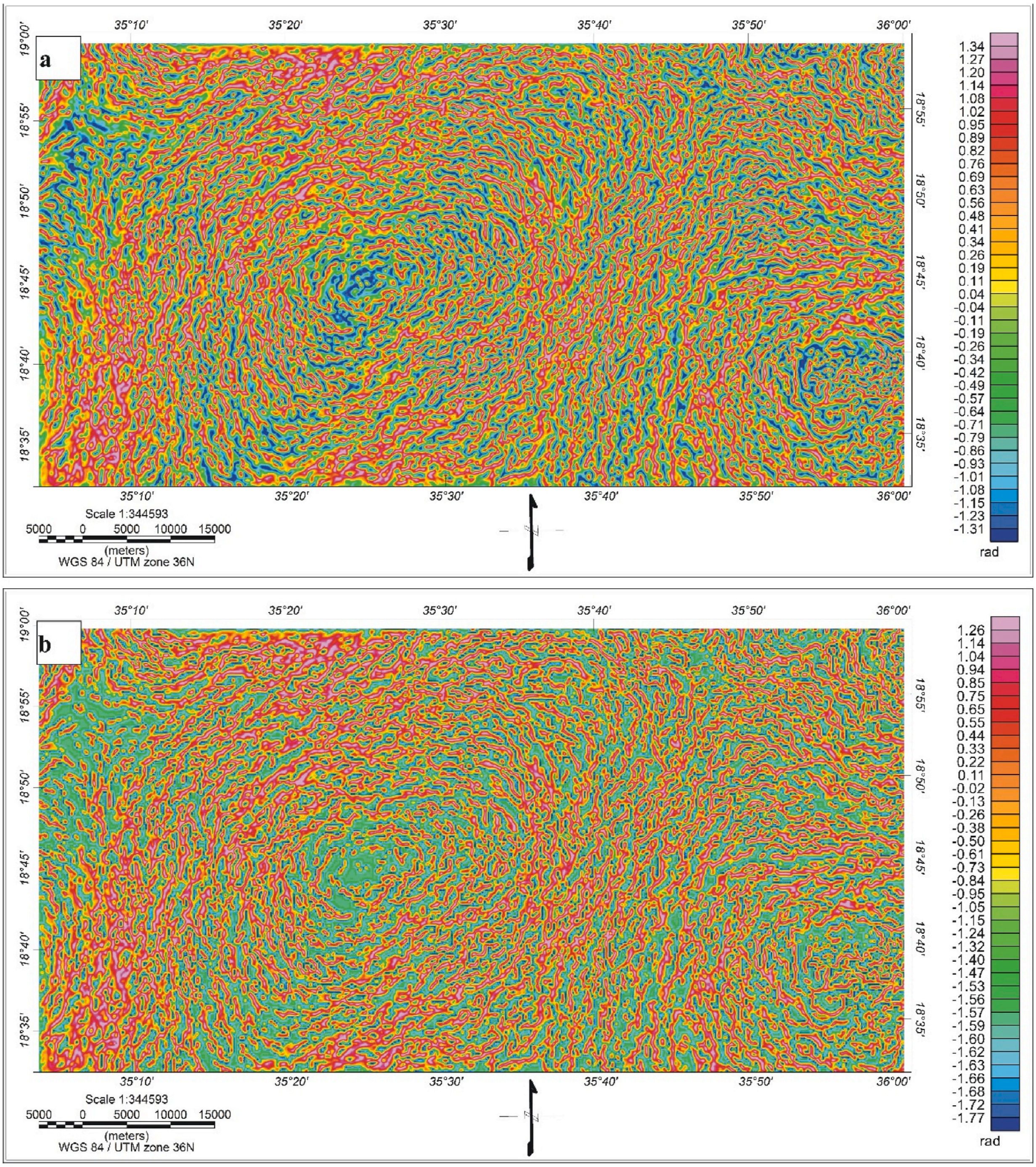

Fig. 11. Tilt Angle of the Horizontal Gradient (TAHG) map; (b) Enhanced Horizontal Gradient Amplitude (EHGA) map of the study area.

discriminated against all the rock units, subsequently highlighting rock unit (C- UFR), particularly the upper felsic rocks and quartz-rich rocks. These rocks are spatially associated with barite deposits in the study area and, thus considered highly important. Fig. 5b clearly highlights barite-bearing rocks in yellow colour.

4.2. Mineralogical indices for barite detection

Based on spectral characteristics of felsic rocks and other accessory alteration minerals within the study area, which is dominated by ferrous oxides, hydroxyl-bearing minerals, iron sulfate minerals, gossans, quartz-rich rocks and carbonates, the following indices

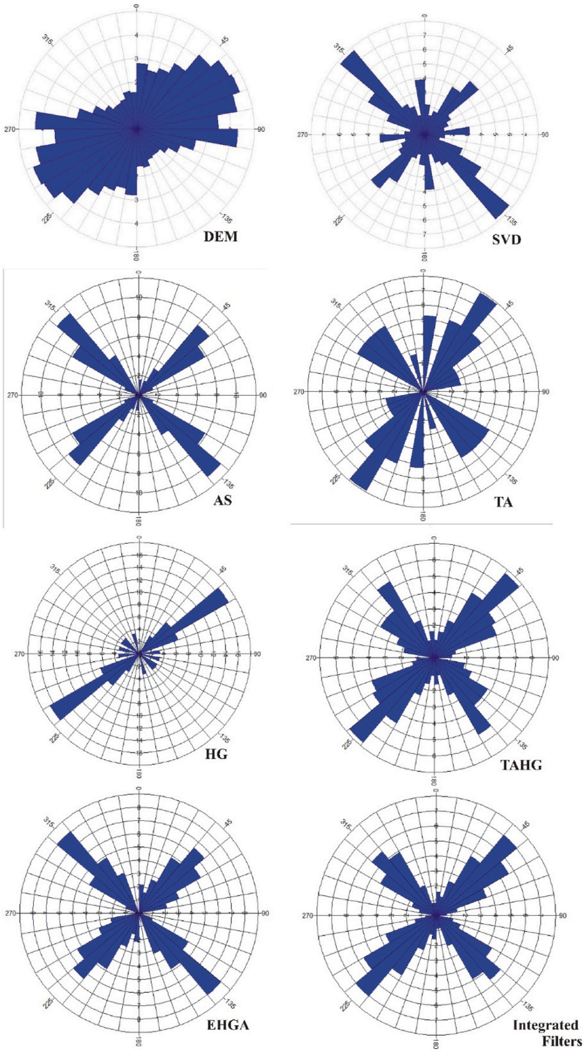

Fig. 12. Rose diagrams illustrate lineament orientations filtered by DEM and gravity datasets revealing predominant trends that align closely with the orientations of major fault structures in the Ariab area.

(Table 4) were used for mapping barite deposits using L8, L9, AST, S2, and PRISMA.

Utilizing L8 and 9, dividing bands (5/6) helps us to map ferrous oxides as shown in Fig. 7a, band ratios of (2/1–5/4) display iron-sulfate minerals (barite) as in Fig. 7b. In contrast, barite content was correctly determined by dividing bands (6/7 + 5/4) which is the high content of barite and silica appears as a white color in the grayscale map (Fig. 7c).

Employing ASTER band ratios specially SWIR, are the most effective bands showing strong absorption features of the gossan, which was detected using L9 and S2 through band ratios of (6/4 in L8 and 6/8A in S2, respectively) as shown in Fig. 8a and b). Furthermore, strong absorption features of the carbonate rocks, especially metasedimentary marble unit (E) by dividing bands (7 + 9/8) as shown in Fig. 8c. All of these mineral assemblages are considered direct or indirect indicators for barite deposits.

4.3. *Structural analysis*

In this study, we achieved a highly effective and more accurate extraction of lineaments by integrating GGMplus data, particularly utilizing the SVD, HG, AS, TA, TAHG, and EHGA filters.

The GGMplus data is equivalent to free-air anomaly (Fig. 9a), to obtain the Bouguer anomaly the SRTM2gravity model was utilized (Fig. 9b). The SRTM2gravity model, an ultra-high-resolution model for gravimetric terrain correction, represents the gravitational attraction of Earth's global topographic masses. It uses data converted from a global 90 m Digital Elevation Model (DEM) from the Shuttle Radar Topography Mission (SRTM) (Hirt et al., 2019). This model implicitly includes the effect of the Bouguer shell and all residual gravity terrain effects calculated with a constant mass density of 2670 kg/m^3.

The Bouguer anomaly map was derived by subtracting the SRTM2gravity data from the Free Air anomaly (Fig. 10a). Following this,

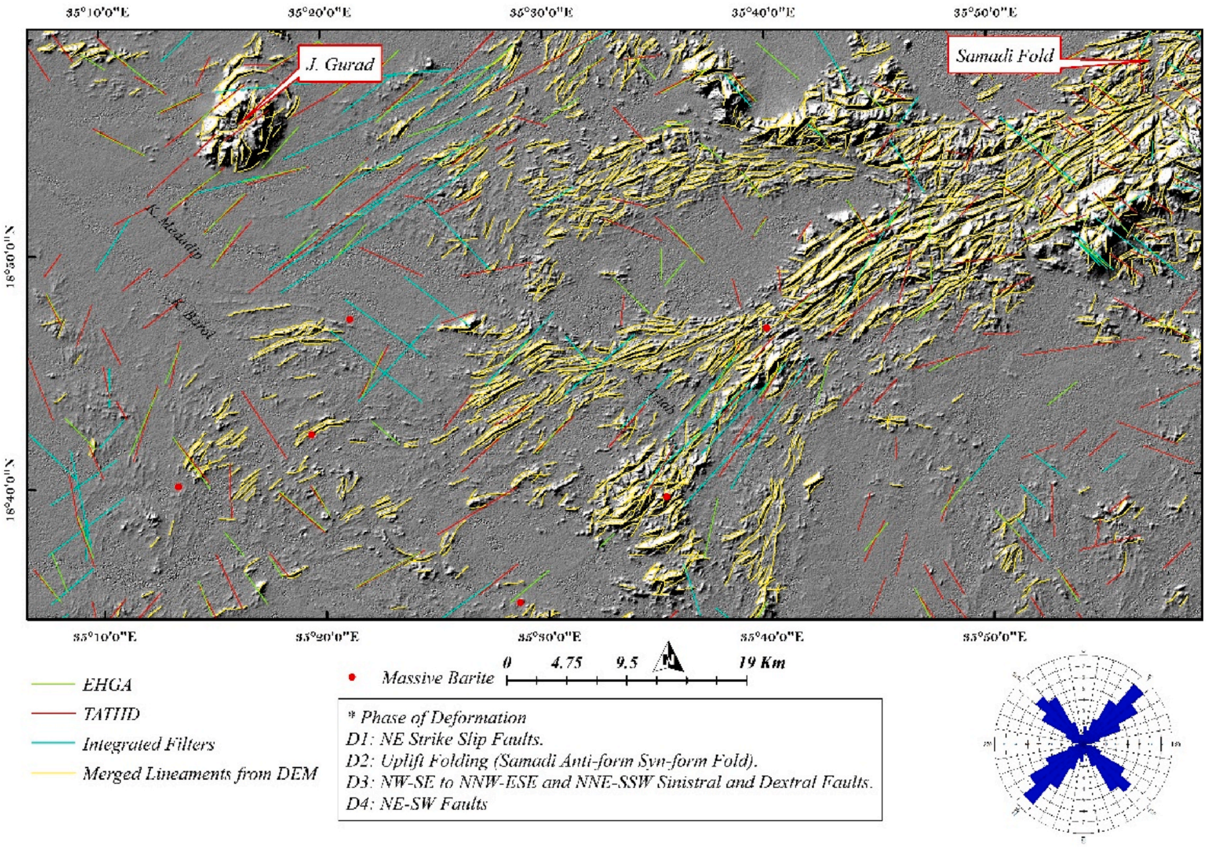

Fig. 13. Extracted linemants from DEM and Gravity with major fault orientations, including NE-SW, NNW-SSE, and NW-SE (Rose diagram).

the AS was computed to highlight boundary zones of varying densities (Fig. 10b). HG method was then applied to delineate density boundaries directly related to subsurface structures (Fig. 10c). Finally, the inclination of the field was measured to enhance structural interpretation, with results illustrated in Fig. 10d. Additional advanced filters were also applied to improve accuracy in boundary delineation. The TAHG filter was used to accentuate horizontal boundaries of buried structures, as shown in Fig. 11a. Furthermore, the EHGA filter was applied to delineate both shallow and deep geological contacts responsible for the observed surface gravity anomalies, as illustrated in Fig. 11b. These advanced filtering techniques greatly improve the clarity and resolution of structural and lithological boundaries, allowing more detailed and accurate mapping of subsurface features and boundary zones within the study area. This multi-step processing approach provides a comprehensive framework for interpreting structural analysis of complex geological environments.

The integration of all previously applied filters successfully delineated the structural framework of the Ariab area, revealing that the predominant trends among these lineaments align closely with major fault orientations, including NE-SW, NNW-SSE, NW-SE, ENE, and NNE, with rose diagrams as illustrated in Fig. (12), Additionally, the automatic extraction was performed on merged DEM map, further enhancing the precision and efficiency of the lineament detection process (Fig. 13), these lineaments, which signify linear geological features indicative of subsurface structures, were subjected to thorough analysis and processing.

Using an integrated suite of filters on the gravity data, all trending deformations within the study area have been delineated with high anomalies in the major trending NE-SW and NW-SE within the Nakasib suture, whereas DEM extraction, generally focused on the minor lineaments and shear zones which mainly trend NE-SW (Fig. 14a), although gravity data focused on all trending deformations within the study area when using an integration of (SVD, HG, AS, TA, TAHG, and EHGA) filters (Fig. 14b). Our findings derived from the integration of different filters on Bouguer anomalies of gravity data with the extraction of lineament from DEM, aligning with previous studies, confirming the dominant trends in the region: NE-SW, NNW-SSE, NW-SE, ENE, and NNE orientations. This consistency with the works of Abdelsalam (2010); Abdelsalam and Stern (1993); Abu-Fatima et al. (2021); Fritz et al. (2013); Johnson et al. (2003); Tucker Barrie (2009) highlights the reliability of our approach. The use of gravity data integrated with DEM enhances the precision of lineament delineation, offering a more detailed understanding of the regional tectonic framework.

A notable example of the (D2) folding system, occurring within the low-grade metamorphism within the Nakasib suture (Northern eastern part), is the Samadi anti-form syn-form fold, as shown in Fig. 15. This fold exhibits a remarkable transgressive sinistral movement, transitioning from NW-SE to NNW-ESE directions, as well as a dextral movement along NNE-SSW orientations within ductile to brittle shear zones.

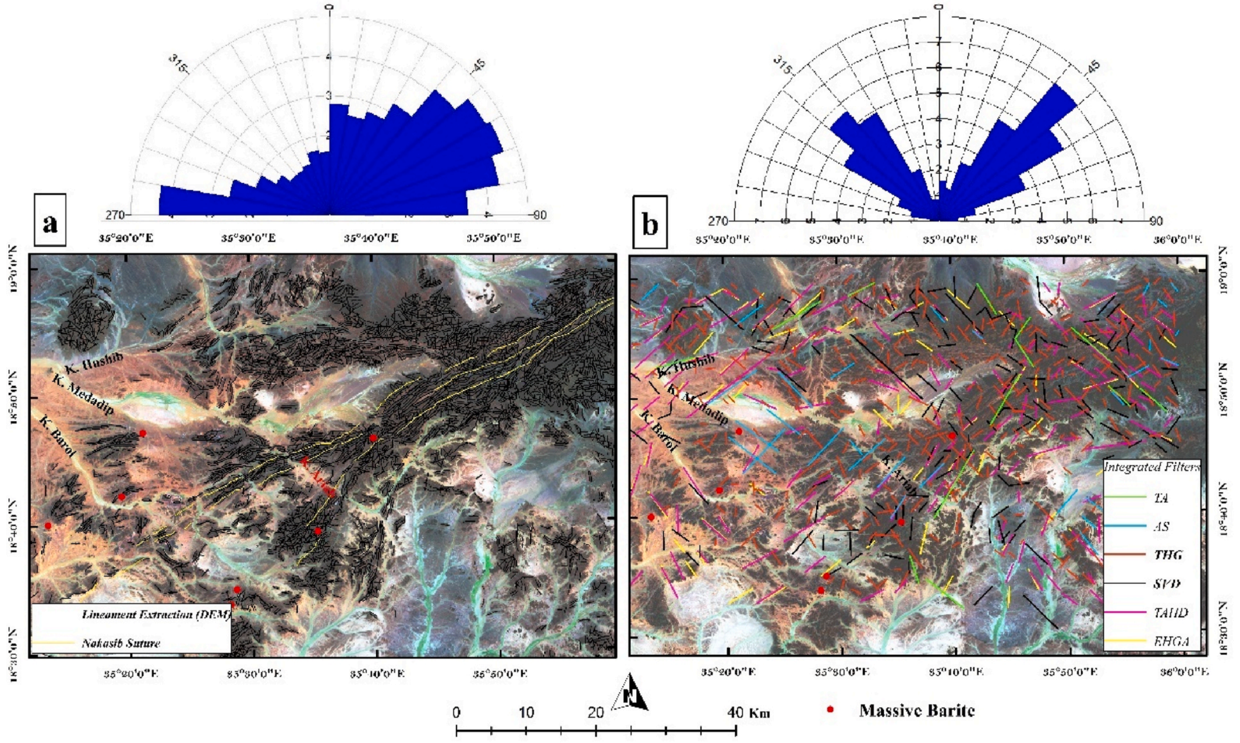

Fig. 14. Lineament extraction with rose diagram from (a) DEM lineament extraction showing predominantly of NE trending strike-slip deformation (D1); (b) predominantly of sinistral (NW-SE to NNW-ESE) and dextral (NNE-SSW) shear zones (D3), red dots referred to barite samples. (For interpretation of the references to colour in this figure legend, the reader is referred to the Web version of this article.)

Through systematic analysis and processing of gravity data using filters, the lineaments, which represent linear geological features indicative of subsurface structures, are extracted and characterized.

The most interesting results from our findings reveal a good correlation with previous studies done in the Samadi area (Abdelsalam, 2010; Johnson et al., 2003). These studies highlighted the dominance of felsic rocks, particularly Unit C2, which are characterized by a high content of massive barite deposits. In our analysis, these barite-rich felsic rocks are prominently marked in yellow in Fig. 15, corroborating earlier geological surveys and emphasizing the significant presence of barite within this lithological unit.

4.4. *Barite potentiality*

In the study area, barite typically occurs in association with metallic ore deposits (such as gold) within the host rocks of Unit C, a felsic volcanic unit ranging from rhyodacitic to rhyolitic compositions, particularly in C2, the primary host for massive sulfide deposits (including gold-bearing massive barite and hematite schists). With the integration of DEM and geophysical gravity data for the lineament and structural extraction, and that of the previous studies, it can be stated that the formation of the barite deposits is influenced by various structural features controlling mineralization. These include mineralization within faults and fractures through which hydrothermal sub-seafloor metamorphism fluid movement during the final collision of the Red Sea Hills (D3) and the rifting of Red Sea (D4); these fractures predominantly trend along NE-SW faults.

The process of barite mineralization is further explained by the detailed investigations employing the integration of DEM and gravity data. This process involves a comparison of our results to previous studies as described in Table 3; the fractionation of supergene collapse structures (D4), which is subsequently influenced by sinistral (northwest-southeast to north-northwest-east-southeast) and dextral (north-northeast-south-southwest) ductile to brittle shear zones (D3) (see Fig. 3a and 14b). These shear zones, in turn, interact with the formation of upright folds (D2) (Fig. 15). Such complex geological phenomena, driven by arc accretion and crustal thickening, have been highlighted in all previous studies, thereby offering a comprehensive understanding of the barite mineralization as depicted in Figs. 14 and 18.

Besides the findings from multispectral data, PRISMA hyperspectral analysis was conducted to unveil the characteristic components of Ariab district lithologies. Applying different image processing such as FCC, PCA, ICA, and MNF of PRISMA highlights the barite occurrences as shown in Fig. 16. False colour composite of bands 226-45-12 in RGB for the specific part (barite-rich) of the study area discriminated against the lithological rock units as in Fig. 16a. PC5 shows the barite bearing lithologies in dark red color (Fig. 16b), MNF 5 is found to be the best for delineating the barite content as illustrated in Fig. 16c, and IC 9 visualized in a color map the distribution of barite bearing rocks (high barite content as purple color) as in Fig. 16d.

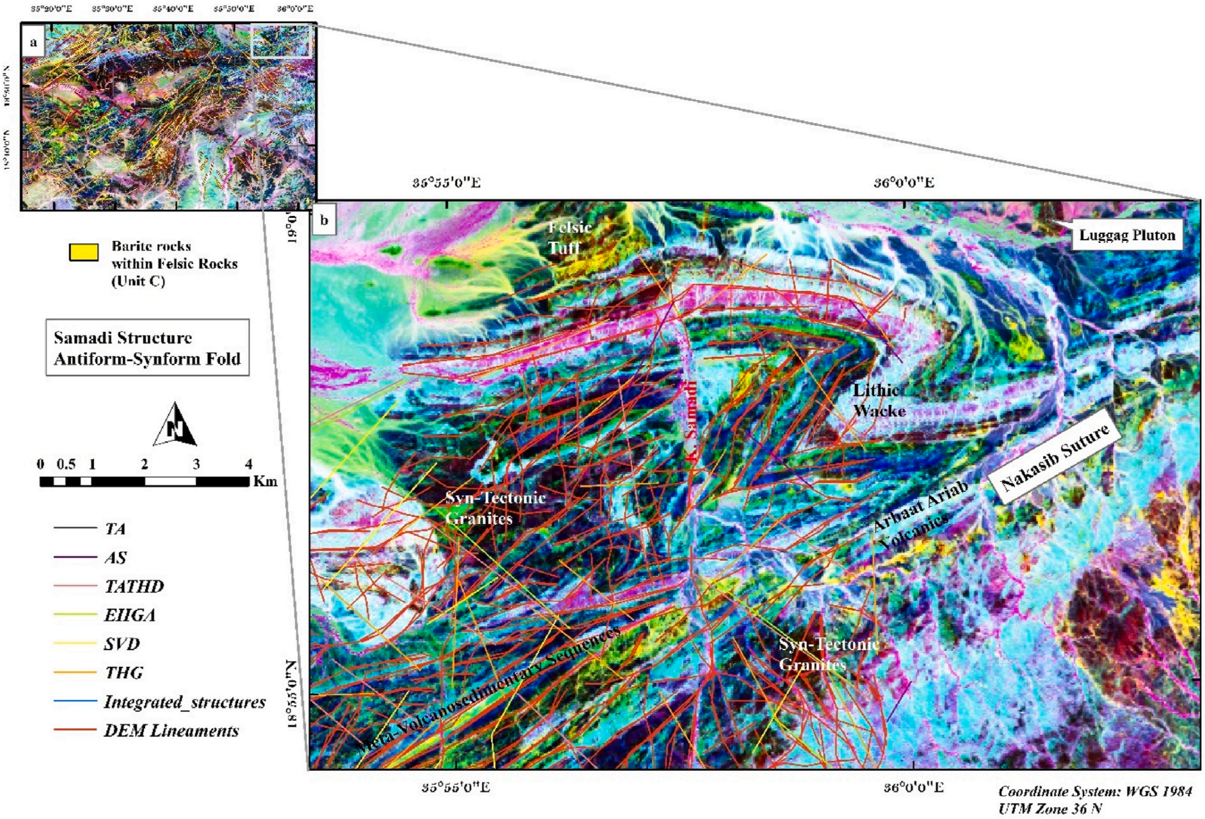

Fig. 15. The Samadi anti-form syn-form fold representing the (D2) type of deformation contains mainly felsic rocks (C) units.

Several spectral elements were investigated for different lithological and mineralogical components using resampled spectral libraries. Our analysis revealed the dominance of iron oxides, silicates, and barite (especially in Unit C). Due to the coarser spatial resolution of PRISMA data, the spectral representation of each pixel is expected to be spectrally complicated (as depicted by the red curve in Fig. 17) due to the contribution of several rock-forming minerals in its pattern. However, a close-up comparison of the characteristic absorption features revealed the presence of goethite, quartz, and barite which was later confirmed by our field investigations.

Investigating the spectral curves of PRISMA with goethite showed a strong resemblance in the characteristic absorption features and an overall coincidence between the two curves, reflecting the dominance of iron oxides. More detailed investigations of barite reflected the best matching (with a wide absorption trough around 900 nm) with PRISMA data. Moreover, a general coincidence in the curve over a considered part (480 nm–950 nm) of the VNIR area was observed between PRISMA and the barite curve. This resemblance in such characteristic features reveals the presence of barite minerals within the investigated pixels. Quartz was also well represented, especially by comparing the SWIR range (2100–2400 nm), where a general coincidence was evident, along with a unique deep absorption trough around 1400 nm.

Our study findings situate closely with the previous geological mapping conducted in the Ariab area when using the best band ratio (2/1–5/4) which delineated the precise locations of extensive barite deposits (Fig. 18a). This conformity highlights the accuracy and reliability of integration of gravity data in identifying and delineating the structurally controlled massive barite occurrences with mineralization (Fig. 18b). The false composite band ((6/7–5/4)6/7–5/6) and ((2/1–5/4)-6/7–5/6) in RGB of L8 and L9, respectively, are the best for detecting potentiality of hydrothermal barite deposits within the selected area and can be used for further exploration in other similar areas (Fig. 18c).

The combination of multi-sensor remote sensing L8, L9, ASTER, S2, and PRISMA highlights the unique spectral characteristics of the hydrothermal massive barite deposits within the study area, equivalent to felsic rocks (unit C) suggests a consistency in the spectral profile of barite across the PRISMA, emphasize our confidence in the accuracy of these results as illustrated (Fig. 19); however, field observations and sampling offer ground truth data that validate and enhance the interpretation of remote sensing data. Our initial field observations were conducted on March 16, 2024, to collect samples based on previous findings. Subsequent field trips were undertaken to measure the strike and dip directions of extracted lineaments from gravity data and to collect barite samples from various parts of the study area, as depicted in Fig. 20.

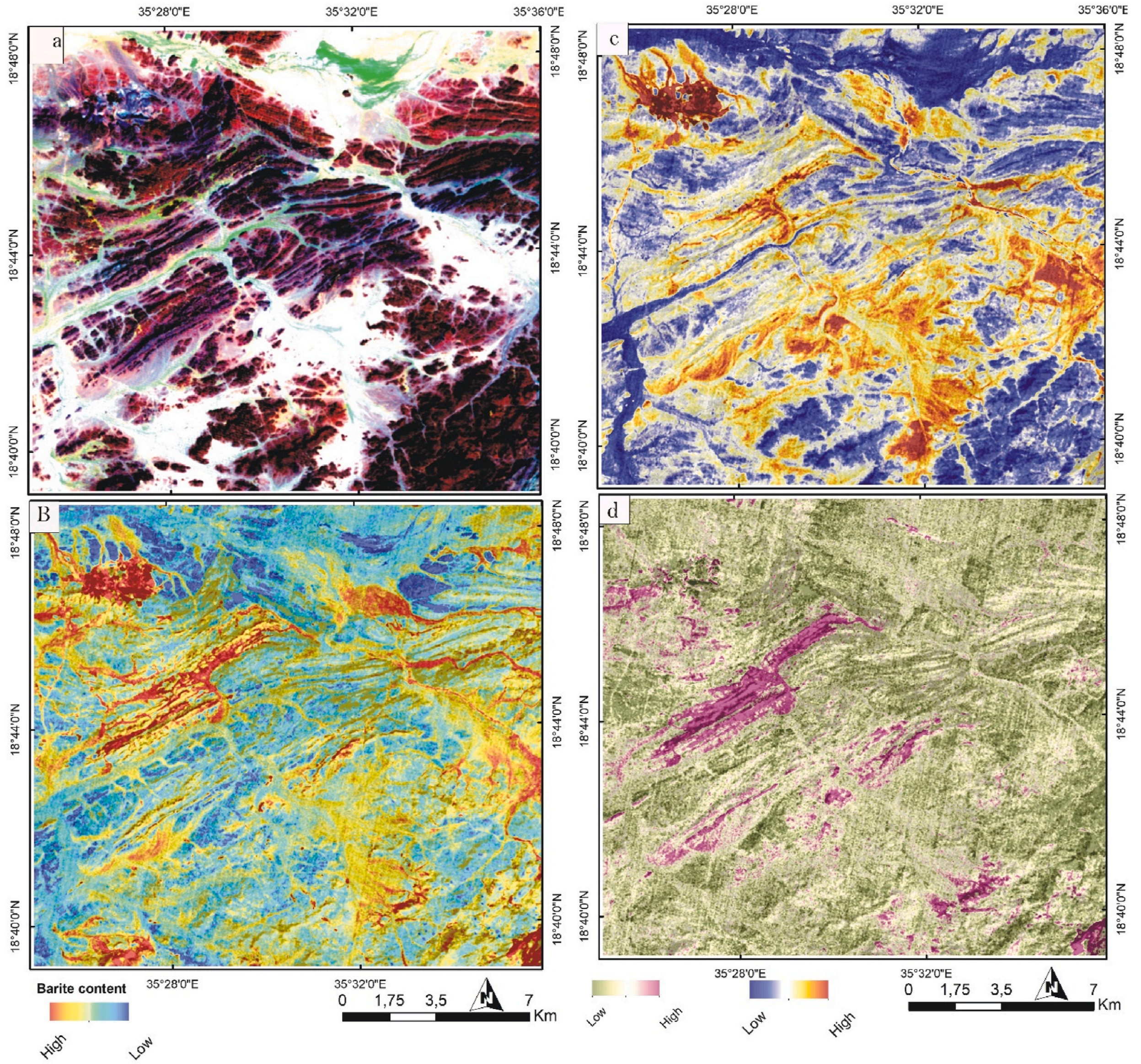

Fig. 16. PRISMA images showing (a) False colour composite (226-45-12 in RGB) of the selected part of the study area. Visualization for the distribution of barite-bearing rocks in a color map of (b) PC5; (c) MNF and (d) IC 9. (For interpretation of the references to colour in this figure legend, the reader is referred to the Web version of this article.)

5. Discussion

The Neoproterozoic crust of the ANS, particularly in northeastern Sudan, hosts various mineral deposits, with the Ariab area being a significant source of barite and silica barite rocks (SBR). These deposits are primarily associated with orogenic gold, which is linked to volcanic massive sulfides (VMS) in the felsic volcanic unit of rhyodacitic to rhyolitic compositions (Unit C- UFR) (Abdelrahman et al., 2024; Abu-Fatima et al., 2021; Adam et al., 2024; Barrie et al., 2016). Beyond its geological significance, barite has distinctive implementations in different medical, environmental, and engineering applications. These multifaceted applications underscore the wide importance of understanding its formation, distributions, and delineations.

In the selected study area, barite occurs in close association with gold mineralization through five major associations: (1) interconnected massive barite and exhalative hematite-magnetite schists (SBR); (2) volcanic-hosted massive sulfide deposits (VHMS); (3) pre-orogenic quartz veins; (4) carbonate-pyrite-quartz alteration zones; and (5) supergene gold enrichment zones (Johnson et al., 2017). SBR as a result of oxidation of VMS deposits serves as a descriptive term for supergene origin micro-breccias adjacent to iron-rich facies 'gossans' and classified geologically into three primary categories ferruginous, jarositic and sugary (Abu-Fatima et al., 2021), the age of the deposits, determined through lead isotope data, dates back approximately 702 ± 15 million years (Barrie et al.,

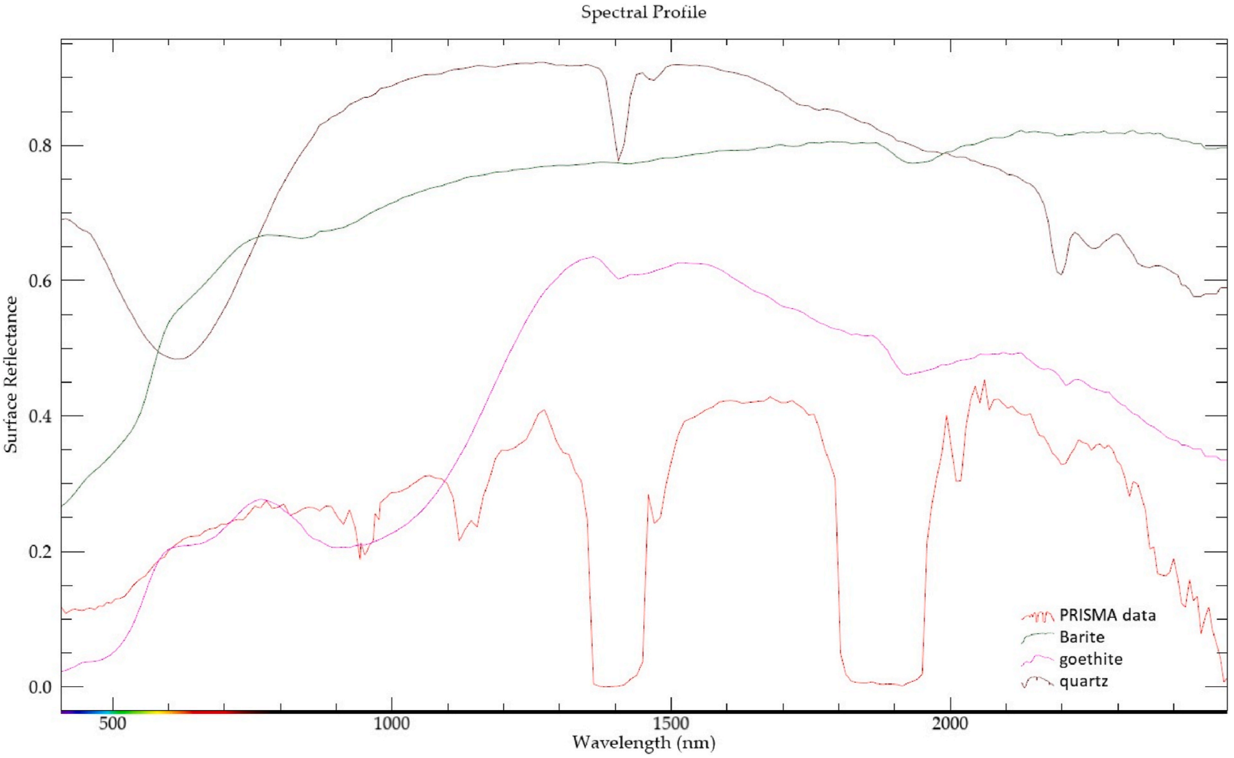

Fig. 17. PRISMA hyperspectral profile showing the dominance of goethite, quartz, and barite (Red curve represents spectral PRISMA data). (For interpretation of the references to colour in this figure legend, the reader is referred to the Web version of this article.)

2016).

The application of hyperspectral PRISMA and multispectral L9, L8, ASTER, and S2 with integration of gravity data revealed significant associations between the barite mineralization and metallic ore deposits, particularly gold, within the felsic volcanic unit (Unit C). This association aligns with all previous research done in the selected study area and similar areas within the Arabian Nubian Shield which identified the felsic volcanic rock unit as a significant host for the VMS oxide gold deposits (Abdelrahman et al., 2024; Adam et al., 2024). A key outcome of this study is the successful distinction of lithological units in the study area, achieved for the first time using integrated hyperspectral and multispectral remote sensing and geophysical gravity datasets.

One of the significant contributions of this research is the successful and clear distinction of the delineated lithological units (for the first time over the study area by using these integrated datasets). The integration of multi-sensor hyperspectral and geospatial remote sensing (RS) with geophysical gravity data has been successfully used for detecting hydrothermal barite deposits within the Ariab area, contributing to a new method for lithological and mineral mapping of the region. Techniques, including L9 (6/7–5/4)-6/7–5/6), L8 (2/1–5/4)-6/7–5/6), ASTER (PC6-4-1), S2 (4/2–11/12-4/11) and (12–6/8A-12/11) in RGB respectively, and PRISMA (PC5, MNF5, and IC9), and DEM, combined with gravity data, has been significant in highlighting the unique spectral characteristics of massive barite deposits within the study area.

The structural control of barite mineralization is another key finding of this study. The integration of DEM and geophysical gravity methods for the lineament and structural extraction, and the previous studies highlighted that the formation of barite deposits is influenced by various structural features that control mineralization. These include mineralization during the final collision of the Red Sea Hills (D3) and the rifting of the Red Sea (D4) (Abu-Fatima et al., 2021; Barrie and Hannington, 2019), these fractures predominantly trend along NE-SW faults. Additionally, supergene collapse structures (D4) fractionation followed by sinistral (NW-SE to NNW-ESE) and dextral (NNE-SSW) ductile to brittle shear zone (D3) and upright folds (D2) (see Fig. 14b) due to arc accretion and thickening suggested all previous studies and contribute to the barite mineralization process, as suggested by detailed investigations using integration of DEM and gravity data.

In this study, we achieved highly effective and accurate extraction of lineaments by integrating merged DEM and GGMplus data, with a particular emphasis on integrated filters. The analysis revealed that the predominant trends of these lineaments align with major fault orientations, including NE-SW, NNW-SSE, NW-SE, ENE, and NNE directions representing four phases of deformations within the study area.

The DEM extraction predominantly focused on identifying minor lineaments and shear zones, which are primarily oriented in the NE-SW direction. In contrast, the gravity data, when Bouguer anomalies were processed with TAHG and EHGA filters (see Fig. 11), provided a comprehensive view of all trending deformations within the study area D3 sinistral (NW-SE to NNW-ESE) and dextral (NNE-SSW) ductile to brittle shear zone. Additionally, due to the high specific gravity of barite, we successfully utilized gravity data to

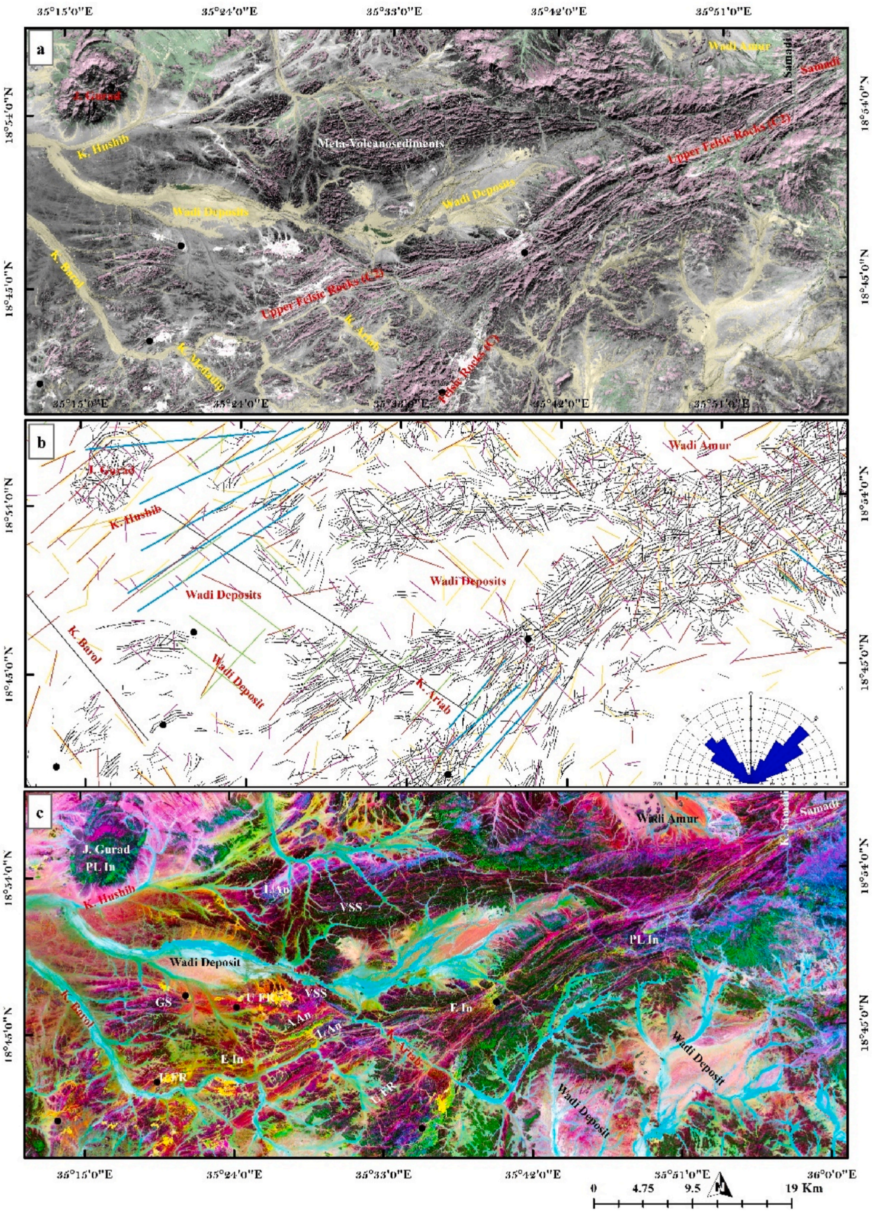

Fig. 18. (a) Potential map displays areas of the high content of barite deposit (6/7–5/4) appearing as a white colour in L8; (b) lineament extraction from gravity dataset; and (c) FCC of L9 (6/7–5/4-6/7–5/6 in RGB) displays barite deposit as a yellow colour. Black dots refer to massive barite samples verified in the field. (For interpretation of the references to colour in this figure legend, the reader is referred to the Web version of this article.)

enhance the detection and characterization of structurally controlled barite mineralization. The gravity data further corroborated the trends identified by the DEM, providing a robust multi-faceted approach to lineament extraction of structurally controlled mineralization.

By comparing our study to recent investigations of barite deposits worldwide using multispectral remote sensing techniques (Madani and Emam, 2011; Rockwell et al., 2021), and using multi-criteria decision models to investigate barite deposits in the Mid-Nigerian Benue Tough (MBT) Nigeria by Gajere et al. (2024); specifically, our research integrates a variety of spectral indices and principal component analyses across different satellite platforms. Previous researchers have utilized techniques such as the coastal aerosol band in L8 for identifying and delineating iron sulfate minerals (Rockwell et al., 2021). Building on this, we employed new band combinations for Landsat 9 (L9) such as (6/7–5/4-6/7–5/6 in RGB) and Landsat 8 (2/1–5/4-6/7–5/6 in RGB). Additionally, we utilized ASTER with principal components (PC6-4-1) and Sentinel-2 (S2) with indices (4/2–11/12-4/11 and 12–6/8A-12/11 in RGB). These were further complemented by hyperspectral data from PRISMA (PC5, MNF5, and IC9) and free satellite gravity data. These

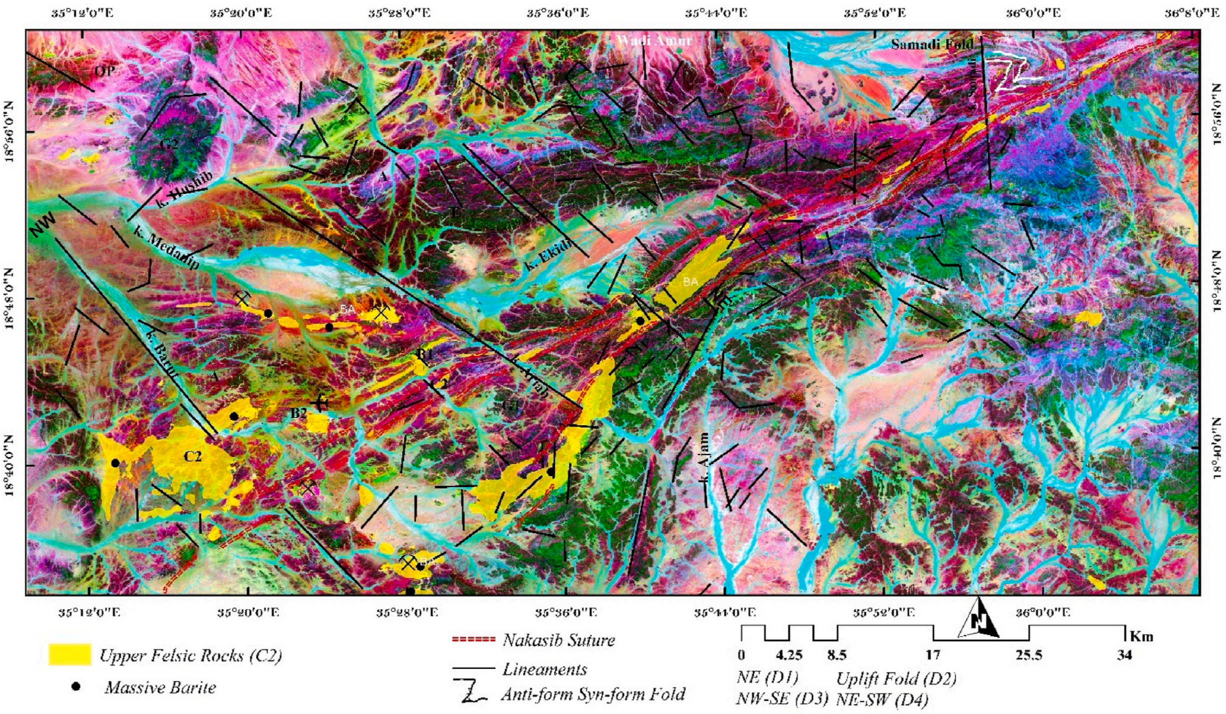

Fig. 19. Distribution of barite-bearing rocks with integration of lineaments from satellite gravity.

Fig. 20. Field photographs showing (a) the hydrothermal massive barite occur as a cap rock of felsic rock units, NE, NW, SW refer to lineament directions; (b) highly fractured massive barite by major Nakasib suture trending NE-SW (D2); (c) hydrothermal massive barite samples containing quartz; and (d) hand specimen of barite samples.

comprehensive methodologies enabled us to detect and delineate high anomalies of barium sulfate deposits, which are characterized by their high specific gravity. By enhancing the spectral analysis techniques and incorporating gravity data, our study offers a more precise and robust approach to identifying barite deposits.

The final modified geological map of the Ariab area with a targeting zone of barite occurrences within the felsic rock units has been generated by the combination of multi-sensor remote sensing with the gravity data as shown in Fig. 21.

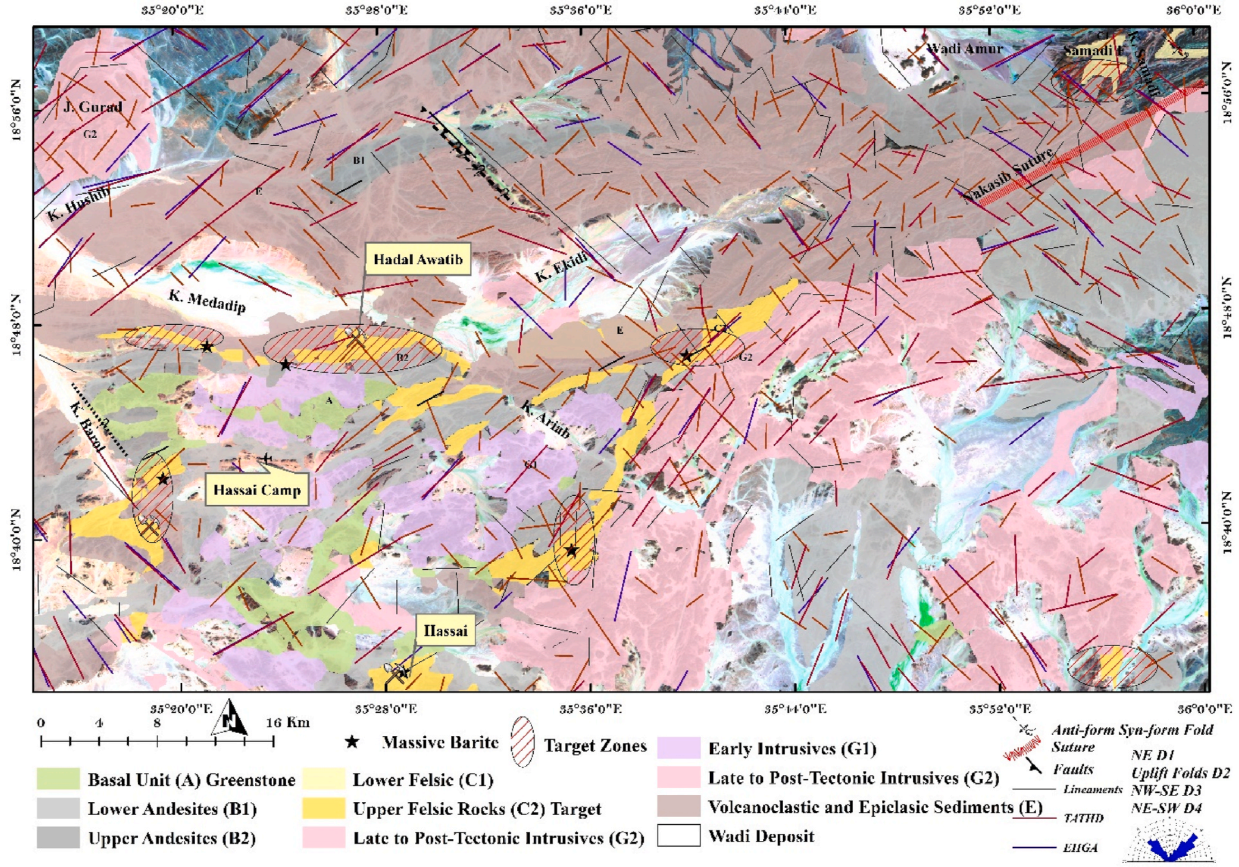

Fig. 21. Final geological map of the Ariab area with targeting zones of massive barite deposit.

6. Conclusion

This study is the first to integrate multispectral (Landsat 9, Landsat 8, Sentinel-2, ASTER), hyperspectral (PRISMA), digital elevation model (DEM), with gravity data for the detection of hydrothermal barite deposits within the Ariab area, Sudan. Our comprehensive approach has proven to be effective in identifying these deposits with detailed lithological units. Our study concludes the following.

- Barite deposits are spatially associated with felsic rocks (C group) and best discriminated by FCC from BR in L9 (6/7–5/4)-6/7–5/6), L8 (2/1–5/4)-6/7–5/6), and ASTER (PC6-4-1).
- PRISMA spectral analysis highlighted that barite deposits are associated with quartz-rich rocks and iron alterations which are confirmed by our field observations.
- The barite deposits within the study area show a strong relationship with phases of deformation (D3) detected by geophysical gravity datasets, indicating that mineralization is structurally controlled. This finding is crucial for understanding the distribution and genesis of barite and gold deposits in the region.
- The generated potential map of barite deposits is highly recommended for guiding further exploration activities and securing barite for further industrial applications.
- For future research, we suggest implementing adopted satellite image combinations and geophysical data to enhance the detection and characterization of mineral deposits.

CRediT authorship contribution statement

Abazar M.A. Daoud: Writing – original draft. **Ali Shebl:** Writing – review & editing, Software, Methodology. **Mohamed M. Abdelkader:** Methodology. **Ali Ahmed Mohieldain:** Methodology, Data curation. **Árpád Csámer:** Validation, Conceptualization. **Albarra M.N. Satti:** Validation, Investigation. **Péter Rózsa:** Writing – review & editing, Supervision.

Declaration of competing interest

The authors declare that they have no known competing financial interests or personal relationships that could have appeared to influence the work reported in this paper.

Acknowledgement

We express our profound gratitude to Eng. Abdelbagi Abdelrahman and Eng. Mohamed Fath for their invaluable assistance in the collection of samples from the study site. Our heartfelt appreciation also extends to the director of Ariab Mining Company (AMC) for their generous support in facilitating access to collect barite samples from the Ariab area.Furthermore, we extend our sincere thanks to the United States Geological Survey (USGS) and the Global Gravity Model Plus (GGMplus) initiative for providing access to critical satellite imagery and geospatial datasets that were instrumental in advancing this research.Finally, we acknowledge with great appreciation the support provided by the Stipendium Hungaricum Scholarship program, a distinguished initiative fostering academic collaboration between Sudan and Hungary, which has been pivotal in enabling this research endeavor.

Data availability

Data will be made available on request.

References

Abdelkareem, M., Al-Arifi, N., 2021. Synergy of remote sensing data for exploring hydrothermal mineral resources using GIS-based fuzzy logic approach. Rem. Sens. 13 (22). https://doi.org/10.3390/rs13224492.

Abdelrahman, S., Ibrahim, M.A.E., Li, H., Abdel Rahman, E.M., Faisal, M., 2024. Geochemical characteristics of neoproterozoic metavolcanic rocks of Ariab auriferous volcanogenic massive sulfide deposit, Red Sea Hills, north-east Sudan. J. Afr. Earth Sci. 216, 105305. https://doi.org/10.1016/j.jafrearsci.2024.105305.

Abdelsalam, M.G., 2010. Quantifying 3D post-accretionary tectonic strain in the arabian-nubian shield: superimposition of the Oko shear zone on the Nakasib suture, Red Sea Hills, Sudan. J. Afr. Earth Sci. 56 (4–5), 167–178. https://doi.org/10.1016/j.jafrearsci.2009.07.003.

Abdelsalam, M.G., Stern, R.J., 1993. Tectonic evolution of the Nakasib suture, Red Sea Hills, Sudan: evidence for a late precambrian wilson cycle. In: Journal of the Geological Society, vol. 1150.

Abdelsalam, M.G., Stern, R.J., 1996. Mapping precambrian structures in the sahara desert with SIR-C/X-SAR radar: the neoproterozoic keraf suture, NE Sudan. J. Geophys. Res.: Planets 101 (E10), 23063–23076. https://doi.org/10.1029/96JE01391.

Abu-Fatima, M., Marignac, C., Cathelineau, M., Boiron, M.C., 2021. Metallogeny of a pan-african oceanic arc: VHMS and gold deposits in the Ariab-Arbaat belt, Haya terrane, Red Sea Hills (Sudan). Gondwana Res. 98, 76–106. https://doi.org/10.1016/j.gr.2021.06.001.

Adam, M.S.M., Babikir, K.A., Kim, Y.J., Park, M.E., F, H., Orellana, J., Kim, Y.S., 2024. Geology and structural setting of the undiscovered Amgififa volcanogenic massive sulfide (VMS) deposit in the southwestern part of the Haya Terrane, Arabian-Nubian Shield, Sudan. Ore Geol. Rev. 167. https://doi.org/10.1016/j.oregeorev.2024.105969.

Ahmadi, H., Pekkan, E., Seyitoğlu, G., 2023. Automatic lineaments detection using radar and optical data with an emphasis on geologic and tectonic implications: a case study of Kabul Block, eastern Afghanistan. Geocarto Int. 38 (1). https://doi.org/10.1080/10106049.2023.2231400.

Al Jaberi, J., Bageri, B., Elkatatny, S., Patil, S., 2022. Primary investigation of barite-weighted water-based drilling fluid properties. ACS Omega. https://doi.org/10.1021/acsomega.2c06264.

Alarifi, S.S., El-Qassas, R.A.Y., Omar, A.E.A., Al-Saleh, A.M., Andráš, P., Eldosouky, A.M., 2024. Remote sensing and aeromagnetic mapping for unveiling mineralization potential: Nuqrah Area, Saudi Arabia. Geomechanics and Geophysics for Geo-Energy and Geo-Resources 10 (1). https://doi.org/10.1007/s40948-024-00844-z.

Ali, E.A., Abdel Rahman, E.M., 2011. New ophiolite occurrences in Sudan and constraint on the western boundary of the Nubian Shield: petrographical and geochemical evidence. J. Afr. Earth Sci. 59 (1), 101–110. https://doi.org/10.1016/j.jafrearsci.2010.09.002.

Ali, H.F., Abu El Ata, A.S.A., Lala, A.M., Youssef, M.A.S., Salem, S.M., 2024. Modeling remote-sensing and geophysical data to delineate the favorable mineralization localities at Semna area, Central Eastern Desert, Egypt. Egyptian Journal of Remote Sensing and Space Science 27 (2), 416–435. https://doi.org/10.1016/j.ejrs.2024.04.010.

Badarloo, B., Lehner, P., Doost, R.B., 2022. Mechanical properties and gamma radiation transmission rate of heavyweight concrete containing barite aggregates. Materials 15 (6). https://doi.org/10.3390/ma15062173.

Barrie, C.T., Abdalla, M.A.F., Hamer, R.D., 2016. Volcanogenic massive sulphide–oxide gold deposits of the nubian shield in northeast Africa. In: Bouabdellah, M., Slack, J.F. (Eds.), Mineral Deposits of North Africa. Springer International Publishing, pp. 417–435. https://doi.org/10.1007/978-3-319-31733-5_17.

Barrie, C.T., Hannington, M.D., 2019. Classification of volcanic-associated massive sulfide deposits based on host-rock composition. In: Volcanic Associated Massive Sulfide Deposits<subtitle>Processes and Examples in Modern and Ancient Settings</subtitle>. Society of Economic Geologists. https://doi.org/10.5382/rev.08.01.

Bencharef, M.H., Eldosouky, A.M., Zamzam, S., Boubaya, D., 2022. Polymetallic mineralization prospectivity modelling using multi-geospatial data in logistic regression: the Diapiric Zone, Northeastern Algeria. Geocarto Int. 37 (27), 15392–15427. https://doi.org/10.1080/10106049.2022.2097481.

Camacho, M., Alvarez, R., 2021. Geophysical modeling with satellite gravity data: Eigen-6C4 vs. GGM plus. Engineering 13 (12), 690–706. https://doi.org/10.4236/eng.2021.1312050.

Chakraborty, R., Rachdi, I., Thiele, S., Booysen, R., Kirsch, M., Lorenz, S., Gloaguen, R., Sebari, I., 2024. A spectral and spatial comparison of satellite-based hyperspectral data for geological mapping. Rem. Sens. 16 (12). https://doi.org/10.3390/rs16122089.

Cordell, L., 2022. Gravimetric Expression of Graben Faulting in Santa Fe Country and the Espanola Basin. New Mexico, pp. 59–64. https://doi.org/10.56577/ffc-30.59.

Daungwilailuk, T., Yenchai, C., Rungjaroenkiti, W., Pheinsusom, P., Panwisawas, C., Pansuk, W., 2022. Use of barite concrete for radiation shielding against gamma-rays and neutrons. Construct. Build. Mater. 326. https://doi.org/10.1016/j.conbuildmat.2022.126838.

Deer FRS, W.A., Howie, R.A., Zussman, J., 2013. An introduction to the rock-forming minerals. Mineralogical Society of Great Britain and Ireland. https://doi.org/10.1180/DHZ.

Eldosouky, A.M., Elkhateeb, S.O., Ali, A., Kharbish, S., 2020. Enhancing linear features in aeromagnetic data using directional horizontal gradient at Wadi Haimur area, South Eastern Desert, Egypt. Carpathian Journal of Earth and Environmental Sciences 15 (2), 323–326. https://doi.org/10.26471/cjees/2020/015/132.

Eldosouky, A.M., El-Qassas, R.A.Y., Pour, A.B., Mohamed, H., Sekandari, M., 2021. Integration of ASTER satellite imagery and 3D inversion of aeromagnetic data for deep mineral exploration. Adv. Space Res. 68 (9), 3641–3662. https://doi.org/10.1016/j.asr.2021.07.016.

Eldosouky, A.M., Othman, A., Saada, S.A., Zamzam, S., 2024. A new vector for mapping gold mineralization potential and proposed pathways in highly weathered basement rocks using multispectral, radar, and magnetic data in random forest algorithm. Nat. Resour. Res. 33 (1), 23–50. https://doi.org/10.1007/s11053-023-10292-3.

Eldosouky, A.M., Pham, L.T., Duong, V.-H., Kemgang Ghomsi, F.E., Henaish, A., 2022. Structural interpretation of potential field data using the enhancement techniques: a case study. Geocarto Int. 37 (27), 16900–16925. https://doi.org/10.1080/10106049.2022.2120548.

Elkins, T.A., 1951. The second derivative method of gravity interpretation. Geophysics 16 (1), 29–50. https://doi.org/10.1190/1.1437648.

El-Nadi, A.H., 1989. Late precambrian volcanism in NE Sudan and the evolution of the Nubian shield. In: Journal O] A]rtcan Earth ,~ctences, vol. 9. Issue 4.

Elrasheed, A.A., S, S., 2024. Comparing the Capability of multi- and hyperspectral remote sensing data in lithological mapping using machine learning algorithms: a case study from Sudan. EGU General Assembly. https://doi.org/10.5194/egusphere-egu24-5443.

Elsamani, Y., Almuslem, A.A., Tokhi, M. El, 2001. Geology and geotectonic classification of pan-african gold mineralizations in the red sea hills, Sudan. Int. Geol. Rev. 43 (12), 1117–1128. https://doi.org/10.1080/00206810109465064.

Elsayed Zeinelabdein, K.A., Mohamed, E.A., Elsheikh, A.E.M., 2021. Applications of remote sensing and GIS in geological mapping, mineral prospecting and groundwater investigations in the Arabian-Nubian shield: Cases from the Red Sea Hills of NE Sudan. In: Hamimi, Z., Fowler, A.-R., Liégeois, J.-P., Collins, A., Abdelsalam, M.G., Abd EI-Wahed, M. (Eds.), The Geology of the Arabian-Nubian Shield. Springer International Publishing, pp. 659–686. https://doi.org/10.1007/978-3-030-72995-0_25.

Es-Sabbar, B., Essalhi, M., Essalhi, A., Mhamdi, H.S., 2020. Lithological and structural lineament mapping from landsat 8 oli images in ras kammouna arid area (Eastern Anti-Atlas, Morocco). Economic and Environmental Geology 53 (4), 425–440. https://doi.org/10.9719/EEG.2020.53.4.425.

Ferreira, F.J.F., de Souza, J., Bongiolo, A., de Castro, L.G., 2013. Enhancement of the total horizontal gradient of magnetic anomalies using the tilt angle. Geophysics 78 (3), J33–J41. https://doi.org/10.1190/geo2011-0441.1.

Fritz, H., Abdelsalam, M., Ali, K.A., Bingen, B., Collins, A.S., Fowler, A.R., Ghebreab, W., Hauzenberger, C.A., Johnson, P.R., Kusky, T.M., Macey, P., Muhongo, S., Stern, R.J., Viola, G., 2013. Orogen styles in the East African orogen: a review of the neoproterozoic to Cambrian tectonic evolution. In: Journal of African Earth Sciences, vol. 86. Elsevier Ltd, pp. 65–106. https://doi.org/10.1016/j.jafrearsci.2013.06.004.

Gajere, J.N., Adekeye, O.A., Tende, A.W., Aminu, M.D., 2024. GIS-based multi-criteria decision models for barite exploration in Nigeria's Benue Trough. Sci. Rep. 14 (1). https://doi.org/10.1038/s41598-024-63996-8.

Ghoneim, E., Healey, C., Hemida, M., Shebl, A., Fahil, A., 2023. Integration of geophysical and geospatial techniques to Evaluate geothermal energy at Siwa Oasis, western desert, Egypt. Rem. Sens. 15 (21). https://doi.org/10.3390/rs15215094.

Grauch, V.J.S., Cordell, L., 1987. Short Note Limitations of determining density or magnetic boundaries from the horizontal gradient of gravity or pseudogravity data. In: GEOPHYSICS, vol. 52. Issue 1. http://library.seg.org/.

Habashi, J., Jamshid Moghadam, H., Mohammady Oskouei, M., Pour, A.B., Hashim, M., 2024. PRISMA hyperspectral remote sensing data for mapping alteration minerals in Sar-e-Châh-e-Shur region, Birjand, Iran. Rem. Sens. 16 (7). https://doi.org/10.3390/rs16071277.

Heijlen, W., Vos, K., Kartalis, N., Boyce, A.J., Muchez, P., 2024. The formation of vein-type barite (± base metal, gold) deposits in northern Madagascar and its link with Mesozoic Pangean rifting. Miner. Deposita 59 (2), 255–273. https://doi.org/10.1007/s00126-023-01205-8.

Hewson, R.D., Cudahy, T.J., Huntington, J.F., 2001. Geologic and Alteration Mapping at Mt Fitton, South Australia, Using ASTER Satellite-Borne Data.

Hirt, C., Claessens, S., Fecher, T., Kuhn, M., Pail, R., Rexer, M., 2013. New ultrahigh-resolution picture of Earth's gravity field. Geophys. Res. Lett. 40 (16), 4279–4283. https://doi.org/10.1002/grl.50838.

Hirt, C., Yang, M., Kuhn, M., Bucha, B., Kurzmann, A., Pail, R., 2019. SRTM2gravity: an ultrahigh resolution global model of gravimetric terrain corrections. Geophys. Res. Lett. 46 (9), 4618–4627. https://doi.org/10.1029/2019GL082521.

Hosseini, S.A., Keshavarz Faraj Khah, N., Kianoush, P., Arjmand, Y., Ebrahimabadi, A., Jamshidi, E., 2023. Tilt angle filter effect on noise cancelation and structural edges detection in hydrocarbon sources in a gravitational potential field. Results in Geophysical Sciences 14, 100061. https://doi.org/10.1016/j.ringps.2023.100061.

Ibraheem, I.M., Tezkan, B., Ghazala, H., Othman, A.A., 2023. A new edge enhancement filter for the interpretation of magnetic field data. Pure Appl. Geophys. 180 (6), 2223–2240. https://doi.org/10.1007/s00024-023-03249-3.

Johnson, P.R., Abdelsalam, M.G., Stern, R.J., 2003. The Bi˘r Umq-Nakasib suture zone in the Arabian-Nubian shield: AKey to understanding crustal growth in the east african orogen. In: International Association for Gondwana Research, vol. 6, 3.

Johnson, P.R., Zoheir, B., Stern, B., 2017. Gold-bearing volcanogenic massive sulfides and orogenic-gold deposits in the nubian shield subduction across scales view project late neoproterozoic magmatic "Flare-up" along the northern margin of Gondwana view project. Article in South African Journal of Geology. https://doi.org/10.2113/gssajg.120.1.61.

Kassa, M., 2024. Investigating subsurface structural lineaments of the northwest Ethiopian plateau using gravity data. Heliyon 10 (15), e35520. https://doi.org/10.1016/j.heliyon.2024.e35520.

Kröner, A., 1985. Ophiolites and the evolution of tectonic boundaries in the late proterozoic Arabian-Nubian shield of northeast Africa and Arabia. Precambrian Res. 27 (1–3), 277–300. https://doi.org/10.1016/0301-9268(85)90016-6.

Kröner, A., Stern, R.J., 2004. Africa: pan-african Orogeny. In: Encyclopedia of Geology. Elsevier Inc, pp. 1–12. https://doi.org/10.1016/B0-12-369396-9/00431-7.

Laizer, P., Mulibo, G.D., Marobhe, I., 2024. Subsurface linear structures and potential zones of mineralisation of the Iramba-Sekenke greenstone belt, central Tanzania with implications for the structural-controlled mineralisation. J. Afr. Earth Sci. 215. https://doi.org/10.1016/j.jafrearsci.2024.105261.

Lee, J.W., Kweon, D.C., 2020. Assessment of dose reduction and image quality by barium composite shielding in head and chest CT. Radiat. Eff. Defect Solid 175 (9–10), 809–826. https://doi.org/10.1080/10420150.2020.1768391.

Lu, Y., Yang, C., He, R., 2022. Towards lithology mapping in semi-arid areas using time-series Landsat-8 data. Ore Geol. Rev. 150. https://doi.org/10.1016/j.oregeorev.2022.105163.

Madani, A.A., Emam, A.A., 2011. SWIR ASTER band ratios for lithological mapping and mineral exploration: a case study from El Hudi area, southeastern desert, Egypt. Arabian J. Geosci. 4 (1), 45–52. https://doi.org/10.1007/s12517-009-0059-8.

Mahdi, A.M., Eldosouky, A.M., El Khateeb, S.O., Youssef, A.M., Saad, A.A., 2022. Integration of remote sensing and geophysical data for the extraction of hydrothermal alteration zones and lineaments; Gabal Shilman basement area, Southeastern Desert, Egypt. J. Afr. Earth Sci. 194, 104640. https://doi.org/10.1016/j.jafrearsci.2022.104640.

Marzouki, A., Dridri, A., 2024. Dolomite, quartzite, and sand indices defined for PRISMA hyperspectral data. Application to the Tamlalet inlier (Eastern High Atlas, Morocco). Adv. Space Res. https://doi.org/10.1016/j.asr.2024.09.070.

Miller, H.G., Singh, V., 1994. Potential field tilt a new concept for location of potential field sources. In: Journal of Applied Geophysics, vol. 32.

Mohamed El-Desoky, H., Soliman, N., Ahmed Heikal, M., Moustafa Abdel-Rahman, A., 2021. Mapping hydrothermal alteration zones using ASTER images in the Arabian–Nubian shield: a case study of the northwestern Allaqi district, south eastern desert, Egypt. J. Asian Earth Sci. X, 5. https://doi.org/10.1016/j.jaesx.2021.100060.

Nabighian, M.N., 1972. The analytic signal of two-dimensional magnetic bodies with polygonal cross-section: ITS PROPERTIES AND USE FOR AUTOMATED ANOMALY INTERPRETATION t. In: GEOPHYSICS, vol. 37. Issue 3. http://library.seg.org/.

Ninomiya, Y., Fu, B., 2019. Thermal infrared multispectral remote sensing of lithology and mineralogy based on spectral properties of materials. In: Ore Geology Reviews, vol. 108. Elsevier B.V, pp. 54–72. https://doi.org/10.1016/j.oregeorev.2018.03.012.

Ninomiya, Y., Fu, B., Cudahy, T.J., 2005. Detecting lithology with advanced spaceborne thermal emission and reflection radiometer (ASTER) multispectral thermal infrared "radiance-at-sensor" data. Rem. Sens. Environ. 99 (1–2), 127–139. https://doi.org/10.1016/j.rse.2005.06.009.

Núñez-Demarco, P., Bonilla, A., Sánchez-Bettucci, L., Prezzi, C., 2023. Potential-field filters for gravity and magnetic interpretation: a review. In: Surveys in Geophysics, vol. 44, pp. 603–664. https://doi.org/10.1007/s10712-022-09752-x, 3 Springer Science and Business Media B.V.

Penaloza, I., Tita, A., McNew, E., Chu, P., 2023. Barite resources, production and recovery using froth flotation: a review. In: Minerals Engineering, vol. 203. Elsevier Ltd. https://doi.org/10.1016/j.mineng.2023.108327.

Pham, L.T., Eldosouky, A.M., Oksum, E., Saada, S.A., 2020. A new high resolution filter for source edge detection of potential field data. Geocarto International 37 (11), 3051–3068. https://doi.org/10.1080/10106049.2020.1849414.

Pohan, A.F., Sismanto, S., Nurcahya, B.E., Lewerissa, R., Koesuma, S., Saputro, S.P., Amukti, R., Saputra, H., Adhi, M.A., 2023. Utilization and modeling of satellite gravity data for geohazard assessment in the Yogyakarta area of Java Island, Indonesia. Kuwait Journal of Science 50 (4), 499–511. https://doi.org/10.1016/j.kjs.2023.05.016.

Pour, A.B., Park, T.Y.S., Park, Y., Hong, J.K., Muslim, A.M., Läufer, A., Crispini, L., Pradhan, B., Zoheir, B., Rahmani, O., Hashim, M., Hossain, M.S., 2019. Landsat-8, advanced spaceborne thermal emission and reflection radiometer, and WorldView-3 multispectral satellite imagery for prospecting copper-gold mineralization in the northeastern Inglefield Mobile Belt (IMB), northwest Greenland. Rem. Sens. 11 (20). https://doi.org/10.3390/rs11202430.

Pratama, I.P.D., Osawa, T., As-Syakur, A.R., 2023. Identification of fault zone in bali using GGMPlus gravity and alos-2 palsar-2 data. JURNAL GEOGRAFI 15 (1), 46. https://doi.org/10.24114/jg.v15i1.40772.

Rexer, M., Hirt, C., Bucha, B., Holmes, S., 2018. Solution to the spectral filter problem of residual terrain modelling (RTM). J. Geodesy 92 (6), 675–690. https://doi.org/10.1007/s00190-017-1086-y.

Rockwell, B.W., Gnesda, W.R., Hofstra, A.H., 2021. Improved Automated Identification and Mapping of Iron Sulfate Minerals, Other Mineral Groups, and Vegetation Using Landsat 8 Operational Land Imager Data, San Juan Mountains, Colorado, and Four Corners Region.

Roest, W.R., Verhoett, J., Pilkington, M., 1992. Magnetic interpretation using the 3·0 analytic signal. In: GEOPHYSICS, vol. 57. I. http://library.seg.org/.

Rowan, L.C., Mars, J.C., 2003. Lithologic mapping in the mountain pass, California area using advanced spaceborne thermal emission and reflection radiometer (ASTER) data. Rem. Sens. Environ. 84 (3), 350–366. https://doi.org/10.1016/S0034-4257(02)00127-X.

Russ, J.C., N, F.B., 2016. The Image Processing Handbook, seventh ed. vol. 8. Comput Phys.

Saleh, A., Gabr, S.S., 2024. Application of magnetic data and satellite spectral imaging in identifying gold mineralization zones and its associated subsurface structures at Fawakheir-Attala area, Central Eastern Desert, Egypt. Environ. Earth Sci. 83 (17). https://doi.org/10.1007/s12665-024-11776-y.

Shebl, A., Abdellatif, M., Badawi, M., Dawoud, M., Fahil, A.S., Csámer, Á., 2023. Towards better delineation of hydrothermal alterations via multi-sensor remote sensing and airborne geophysical data. Sci. Rep. 13 (1). https://doi.org/10.1038/s41598-023-34531-y.

Shebl, A., Abriha, D., Dawoud, M., Ali Hussein Ali, M., Csámer, Á., 2024. PRISMA vs. Landsat 9 in lithological mapping − a K-fold Cross-Validation implementation with Random Forest. Egyptian Journal of Remote Sensing and Space Science 27 (3), 577–596. https://doi.org/10.1016/j.ejrs.2024.07.003.

Shebl, A., Csámer, Á., 2021. Reappraisal of DEMs, Radar and optical datasets in lineaments extraction with emphasis on the spatial context. Remote Sens. Appl.: Society and Environment 24. https://doi.org/10.1016/j.rsase.2021.100617.

Shebl, A., Hamdy, M., 2023. Multiscale (microscopic to remote sensing) preliminary exploration of auriferous-uraniferous marbles: a case study from the Egyptian Nubian Shield. Sci. Rep. 13 (1). https://doi.org/10.1038/s41598-023-36388-7.

Soliman, A., Han, L., 2019. Effects of vertical accuracy of digital elevation model (DEM) data on automatic lineaments extraction from shaded DEM. Adv. Space Res. 64 (3), 603–622. https://doi.org/10.1016/j.asr.2019.05.009.

Sono, P., Selepeng, A.T., Mizunaga, H., Akinyemi, F., 2024. Geological mapping and mineral exploration in Francistown region, north east Botswana from integration of ASTER TIR and aeromagnetic data. J. Afr. Earth Sci. 214, 105270. https://doi.org/10.1016/j.jafrearsci.2024.105270.

Sorrentino, A., Chirico, R., Corrado, F., Laukamp, C., Di Martire, D., Mondillo, N., 2024. The application of PRISMA hyperspectral satellite imagery in the delineation of distinct hydrothermal alteration zones in the Chilean Andes: the Marimaca IOCG and the Río Blanco-Los Bronces Cu-Mo porphyry districts. Ore Geol. Rev. 167. https://doi.org/10.1016/j.oregeorev.2024.105998.

Stern, R.J., Abdelsalam, M.G., 1998. Formation of juvenile continental crust in the Arabian-Nubian shield: evidence from granitic rocks of the Nakasib suture, NE Sudan. In: Geol Rundsch, vol. 87.

Stern, R.J., Johnson, P.R., Kröner, A., Yibas, B., 2004. Neoproterozoic ophiolites of the Arabian-Nubian shield. In: Developments in Precambrian Geology, vol. 13, pp. 95–128. https://doi.org/10.1016/S0166-2635(04)13003-X. C.

Stern, R.J., Kroner, A., 1993. Late Precambrian crustal evolution in NE Sudan: isotopic and geochronologic constraints. J. Geol. 101 (5), 555–574. https://doi.org/10.1086/648249.

Stern, R.J., Kroner, A., Manton, W.I., Reischmann, T., Mansour, M., Hussein, I.M., 1989. Geochronology of the late Precambrian Hamisana shear zone, Red Sea Hills, Sudan and Egypt. J. Geol. Soc. 146 (6), 1017–1029. https://doi.org/10.1144/gsjgs.146.6.1017.

Tucker Barrie, C., 2009. Hadal Awatib east Cu-Au VMS deposit, Sudan resource estimates NI 43-101 technical report. https://doi.org/10.13140/RG.2.1.1977.4883.

Vail, J.R., 1990. *Geochronology Of the Sudan*. H.M.S.O.

Van der Meer, F.D., van der Werff, H.M.A., van Ruitenbeek, F.J.A., 2014. Potential of ESA's Sentinel-2 for geological applications. Rem. Sens. Environ. 148, 124–133. https://doi.org/10.1016/j.rse.2014.03.022.

van der Meer, F.D., van der Werff, H.M.A., van Ruitenbeek, F.J.A., Hecker, C.A., Bakker, W.H., Noomen, M.F., van der Meijde, M., Carranza, E.J.M., de Smeth, J.B., Woldai, T., 2012. Multi- and hyperspectral geologic remote sensing: a review. In: International Journal of Applied Earth Observation and Geoinformation, vol. 14. Elsevier B.V, pp. 112–128. https://doi.org/10.1016/j.jag.2011.08.002, 1.

van der Werff, H., van der Meer, F., 2015. Sentinel-2 for mapping iron absorption feature parameters. Rem. Sens. 7 (10), 12635–12653. https://doi.org/10.3390/rs71012635.

Zouaghi, T., Harbi, H., 2022. Airborne geophysics and remote sensing of an Nimas-Khadra area, southern Arabian shield: new insights into structural framework and mineral occurrences. Adv. Space Res. 70 (11), 3649–3673. https://doi.org/10.1016/j.asr.2022.08.046.